In-situ Gallium-doping for forming p^+ Germanium-Tin and application in Germanium-Tin PIN photodetector

Wei Wang,[1] Saumitra Vajandar,[2] Sin Leng Lim,[2] Yuan Dong,[1] Vijay Richard D'Costa,[1] Thomas Osipowicz,[2] Eng Soon Tok,[2] and Yee-Chia Yeo.[1]

[1] *Department of Electrical and Computer Engineering, National University of Singapore, Singapore 117576.*

[2] *Department of Physics and Yale-NUS College, National University of Singapore, Singapore 117551.*

Tel: +65-65162298, Email: yeo@ieee.org

Corresponding Author: Prof. Yee-Chia Yeo

Address: Department of Electrical and Computer Engineering, National University of Singapore, 10 Kent Ridge Crescent, 119260, Singapore.

Email : yeo@ieee.org

Phone : +65 6516-2298

Fax : +65 6779-1103

This manuscript was accepted by J. Appl. Phys. Click here to see the version of record.

ABSTRACT

The *in-situ* Ga doping technique was used to form heavily p-type doped germanium-tin ($Ge_{1-x}Sn_x$) layers by molecular beam epitaxy (MBE), avoiding issues such as Sn precipitation and surface segregation at high annealing temperatures that are associated with the alternative implant and anneal approach. In this way, an electrically active Ga concentration of up to ~3.2×10^{20} cm^{-3} can be realized for $Ge_{1-x}Sn_x$. The impacts of varying the Ga concentration on the crystalline quality and the mobility of p-type $Ge_{1-x}Sn_x$ were investigated. High crystalline quality $Ge_{0.915}Sn_{0.085}$ can be realized with active Ga concentration of up to ~1.2×10^{20} cm^{-3}. More than 98% of the Sn atoms are located on substitutional lattice sites, although the substitutionality of Sn in p-type $Ge_{1-x}Sn_x$ decreases with increasing Ga concentration. When the Ga concentration introduced is higher than 3.2×10^{20} cm^{-3}, excess Ga atoms cannot be substitutionally incorporated, and segregation of Ga and Sn towards the surface during growth is observed. The *in-situ* Ga-doped $Ge_{0.915}Sn_{0.085}$ epitaxy was integrated in a $Ge_{0.915}Sn_{0.085}$-on-Si PIN photodiode fabrication process, and well-behaved $Ge_{0.915}Sn_{0.085}$/Si PIN junction characteristics were obtained. A large forward-bias current to reverse bias current ratio of 6×10^4 and a low reverse current (dark current) of 0.24 μA was achieved at V_{bias} = -1 V.

Index Terms: *Germanium-Tin, in-situ Ga doping, PIN photodiodes, MBE.*

This manuscript was accepted by J. Appl. Phys. Click here to see the version of record.

I. INTRODUCTION

Germanium-Tin ($Ge_{1-x}Sn_x$) alloy has attracted strong research interests, due to its potential application in field-effect transistors and in optoelectronic devices. It can be used as an alternative channel material for future CMOS, due to its higher electron and hole mobilities than that of Si or Ge.[1-4] It can also be used as an absorption material for infrared detection.[5-10] In addition, recent theoretical calculation and experimental measurements showed that the indirect-to-direct bandgap transition for $Ge_{1-x}Sn_x$ alloys occurs at a Sn composition of around 6% – 11%,[11-15] making it a possible candidate as the gain medium [16,17] in lasers based on Group IV materials.

With the development of non-equilibrium growth techniques such as molecular beam epitaxy (MBE) and chemical vapor deposition (CVD), $Ge_{1-x}Sn_x$ alloys with x up to 0.34 can be realized.[18-23] However, $Ge_{1-x}Sn_x$ film with high Sn content is not stable under certain thermal annealing conditions,[24,25] which poses a challenge for device fabrication. Low thermal budget is thus required in subsequent device fabrication steps, such as junction formation and surface passivation. In contrast to Si or Ge, dopant characteristics in $Ge_{1-x}Sn_x$ have received limited attention.

Boron is often used as a p-type dopant in Ge. After boron implantation, electrically active concentrations of 2 – 5.7×10^{20} cm^{-3} were demonstrated through solid-phase epitaxial regrowth (SPER).[26-28] We reported that after implantation of boron difluoride BF_2^+ into $Ge_{1-x}Sn_x$ with $x \leq 0.053$, boron can be activated during a 400 °C SPER.[29] However, the crystallinity of the $Ge_{1-x}Sn_x$ was not investigated. Ga is another p-type dopant in Ge, with the equilibrium solubility as high as 4.9×10^{20} cm^{-3} in bulk Ge.[30] Realization of heavily Ga doped Ge was reported with hole densities up to 1.4×10^{21} cm^{-3}.[31,32] An electrically active concentration of 5.5×10^{19} cm^{-3} was also reported in $Ge_{1-x}Sn_x$ by *in-situ* Ga doping technique.[33]

In this paper, *in-situ* Ga doping during the epitaxial growth was developed to form p-type $Ge_{1-x}Sn_x$, avoiding crystal damages caused by the implant and anneal approach. The dependence of crystallinity and mobility of the Ga-doped $Ge_{1-x}Sn_x$ layer on the Ga concentrations were investigated.

This manuscript was accepted by J. Appl. Phys. Click here to see the version of record.

In addition, $Ge_{1-x}Sn_x$ on Si PIN photodiodes (PDs) were fabricated based on the *in-situ* doping technique, with process temperatures lower than 250 °C.

II. EXPERIMENTAL DETAILS

A. Formation and Characterization of P-type $Ge_{1-x}Sn_x$

The $Ge_{1-x}Sn_x$ samples were grown on Ge(001) substrates by a solid-source MBE system with a base pressure of 3×10^{-10} Torr at the National University of Singapore (NUS). After pre-epitaxy cleaning by dilute hydrofluoric acid (DHF) (HF:H_2O = 1:50), the wafers were baked at 630 °C for 5 minutes in the MBE chamber to remove the native oxide. The substrate temperature was then reduced to 150 °C for the $Ge_{1-x}Sn_x$ growth. Ge, Sn, and Ga were all evaporated by using pyrolytic boron nitride (PBN) Knudsen cells. The deposition rates of Ge, Sn, and Ga can be adjusted by tuning the temperatures of the effusion cells. During growth, the Ge deposition rate was fixed, while those of Sn and Ga were adjusted according to the desired composition. To exclude the effect due to strain relaxation, the thicknesses (~40-70 nm) of $Ge_{1-x}Sn_x$ layers are kept below critical thickness [23].

Some $Ge_{1-x}Sn_x$ samples that were undoped during MBE received BF_2^+ implantation with an energy of 20 keV and a dosage of 1×10^{15} cm^{-2}. The implanted samples were then cut into small pieces (~1×1 cm^2) for an anneal study, where rapid thermal annealing (RTA) was performed at various temperatures from 400 – 600 °C near atmospheric pressure in a nitrogen gas ambient.

High resolution x-ray diffraction (HRXRD) and Rutherford backscattering spectrometry (RBS) were used to examine the composition and crystalline quality of the $Ge_{1-x}Sn_x$ layer. Transmission electron microscopy (TEM) was employed to investigate the layer structure, and tapping mode atomic force microscopy (AFM) was used to analyze the surface morphologies of the $Ge_{1-x}Sn_x$ films. Secondary ion mass spectrometry (SIMS) was used to extract the total Ga concentration and infrared ellipsometry was used to evaluate the resistivity and carrier concentration of the $Ge_{1-x}Sn_x$ layers.

This manuscript was accepted by J. Appl. Phys. Click here to see the version of record.

B. Fabrication of $Ge_{1-x}Sn_x$/Si PIN Photodiodes

The $Ge_{0.915}Sn_{0.085}$ sample used for photodiodes fabrication was grown on a commercially available Ge/Si virtual substrate with a customized n^+-doped Si layer (~1000 nm) and undoped Ge buffer (~350 nm). The threading dislocation density in the Ge buffer is of the order of 10^8 cm^{-2}. After the growth of 80 nm undoped $Ge_{0.915}Sn_{0.085}$ and 40 nm *in-situ* Ga doped (~2.1×10^{20} cm^{-3}) $Ge_{0.915}Sn_{0.085}$ by MBE, chlorine-based reactive-ion etching (RIE) was performed to define circular mesas with various diameters. An $(NH_4)_2S$ (24%) aqueous solution was used to passivate the surface of $Ge_{0.915}Sn_{0.085}$ and Ge at room temperature. ~350 nm SiO_2 layer was deposited by plasma-enhanced chemical vapor deposition (PECVD) for antireflection and isolation. After that, the contact region was opened by dry etch followed by wet etch (DHF) to avoid over-etch of the p^+ $Ge_{0.915}Sn_{0.085}$ layer. Finally, 400 nm-thick aluminium (Al) was deposited by magnetron sputtering system, and then patterned and etched to form the top and bottom electrodes of the $Ge_{0.915}Sn_{0.085}$/Si PDs.

III. RESULTS AND DISCUSSIONS

A. BF_2^+ Implantation and Activation during SPER

Although boron can be activated in BF_2^+-implanted $Ge_{1-x}Sn_x$ by a 400 °C SPER,[29] the restoration of the lattice order that was partially destroyed during implantation may require a higher thermal budget than that for dopant activation.[34] The $Ge_{1-x}Sn_x$ samples were annealed at 400 – 600 °C for 5 minutes after BF_2^+ implantation.

Figure 1(a) shows the HRXRD curves of the annealed $Ge_{0.975}Sn_{0.025}$ samples. After 500 °C annealing, well-defined $Ge_{0.975}Sn_{0.025}$ peak and clear thickness fringes can be observed, similar to those of as-grown sample. This suggests that the damage due to the BF_2^+ implant in $Ge_{0.975}Sn_{0.025}$ can be repaired after annealing at 500 °C. With the annealing temperature further increased to 600 °C, the $Ge_{1-x}Sn_x$ peak shifts to the right, indicating loss of Sn in the $Ge_{1-x}Sn_x$ layer, due to Sn precipitation or surface segregation.

This manuscript was accepted by J. Appl. Phys. Click here to see the version of record.

For $Ge_{0.92}Sn_{0.08}$, the HRXRD curves of the annealed samples are shown in Figure 1(b). After the 400 °C anneal, although the $Ge_{0.92}Sn_{0.08}$ peak can be observed, it is broader than that of the as-grown sample. This suggests that high crystalline quality p-type $Ge_{0.92}Sn_{0.08}$ cannot be formed through SPER at 400 °C. With the annealing temperature increased to 500 °C, a shoulder between $Ge_{0.92}Sn_{0.08}$ and Ge peaks appears in the XRD scan, and some islands appear on the surface. These results indicate that Sn surface segregation occurs during the 500 °C SPER.[24] A lower thermal budget is expected to avoid the Sn precipitation and surface segregation in the $Ge_{1-x}Sn_x$ layer with higher Sn composition. It was reported that for $Ge_{1-x}Sn_x$ with x of 0.17, Sn precipitation occurs at 280 °C, which may be even lower than that needed for dopant activation.[35] Thus, the implant and thermal anneal approach may not be suitable for realizing high-quality p-type $Ge_{1-x}Sn_x$ with $x \geq 0.08$.

B. In-situ Ga Doped $Ge_{1-x}Sn_x$ by MBE

The deposition temperature of *in-situ* Ga doped $Ge_{1-x}Sn_x$ layer was kept low (150 °C) in order to incorporate Sn and Ga into the Ge lattice without Sn precipitation or agglomeration. During MBE growth, the Ge and Sn cell temperatures were fixed so that $Ge_{0.915}Sn_{0.085}$ would be grown. The Ga cell temperature $T_{Ga\text{-}cell}$ was tuned from 540 to 820 °C to realize various Ga doping concentrations.

SIMS was used to determine the total Ga concentration with various $T_{Ga\text{-}cell}$. Figure 2 shows the SIMS depth profiles of Ga and Sn with various $T_{Ga\text{-}cell}$. One intrinsic $Ge_{0.915}Sn_{0.085}$ sample was used as a standard for Sn quantification by SIMS. The Sn concentration was first measured by RBS and XRD, and the relative sensitivity factor was extracted and used for determination of Sn content in the Ga doped $Ge_{0.915}Sn_{0.085}$ samples. For $T_{Ga\text{-}cell}$ of up to 740 °C, the Ga and Sn concentrations are uniform in the $Ge_{0.915}Sn_{0.085}$ layers. At $T_{Ga\text{-}cell}$ = 740 °C, the corresponding Ga concentration is ~2.1×10^{20} cm^{-3}. However, when $T_{Ga\text{-}cell}$ is increased to 820 °C, the Ga concentration is higher than 5.6×10^{20} cm^{-3}, and the Ga concentration profile becomes non-uniform, increasing towards the surface. It can be found that the Sn profile also becomes non-uniform for $T_{Ga\text{-}cell}$ of 820 °C [Fig. 2(b)], with

the Sn composition in the $Ge_{1-x}Sn_x$ layer dropping from ~8.5% to 3%. This result suggests significant interaction between the Ga and Sn atoms as the Ga concentration is higher than about 5.6×10^{20} cm^{-3}. When the introduced Ga concentration exceeds the equilibrium solubility of Ga in bulk Ge (~4.9×10^{20} cm^{-3}), excess Ga atoms may interact with Sn atoms, leading to diffusion of Ga and Sn atoms towards the surface during growth.

HRXRD was used to investigate the crystalline quality of the *in-situ* Ga-doped $Ge_{1-x}Sn_x$ layer with various Ga concentrations. Figure 3 shows the HRXRD curves of the $Ge_{1-x}Sn_x$ samples with various $T_{Ga\text{-}cell}$ or Ga concentrations. Well-defined $Ge_{0.915}Sn_{0.085}$ peak and clear thickness fringes can be seen for $T_{Ga\text{-}cell}$ of up to 740 °C or for Ga concentration up to 2.1×10^{20} cm^{-3}. The total Ga concentrations in the $Ge_{0.915}Sn_{0.085}$ samples grown using $T_{Ga\text{-}cell}$ of 540, 640, and 740 °C are 8.0×10^{17}, 1.5×10^{19}, and 2.1×10^{20} cm^{-3}, respectively, corresponding to Ga content of 0.002%, 0.034%, and 0.471%, respectively. The atomic radii of Ge, Ga, and Sn are 0.125, 0.130, and 0.145 nm, respectively.[36] Therefore, for $T_{Ga\text{-}cell}$ of 740 °C and below, the contribution of Ga atoms to the lattice constant of a $Ge_{0.915}Sn_{0.085}$ layer is small because both the Ga concentration and the difference between the atomic radii of Ga and Ge are sufficiently small compared with the concentration and radius of Sn. No obvious shift of the $Ge_{0.915}Sn_{0.085}$ peak can be observed for Ga concentration up to 2.1×10^{20} cm^{-3} (Fig. 4).

Figure 4(a) shows the cross-sectional TEM image of the $Ge_{0.915}Sn_{0.085}$ sample with Ga concentration of 2.1×10^{20} cm^{-3}. No dislocations or Sn clusters can be observed. High resolution TEM images [Figs. 4(b) and 4(c)] depict an atomically smooth or flat top surface and a good $Ge_{0.915}Sn_{0.085}$/Ge interface. The AFM images (10 μm × 10 μm) of the $Ge_{1-x}Sn_x$ samples with various Ga concentrations are shown in Fig. 5. Smooth surfaces can be observed for Ga concentrations of up to 2.1×10^{20} cm^{-3}, with a root-mean-square (RMS) roughness of less than 0.50 nm (~0.17 nm for Ge substrates). These results demonstrate that high crystalline quality p-type $Ge_{0.915}Sn_{0.085}$ can be realized with Ga concentration up to 2.1×10^{20} cm^{-3}.

However, when the Ga concentration is increased to above 5.6×10^{20} cm^{-3}, corresponding to a Ga content of 1.260%, the $Ge_{1-x}Sn_x$ peak shifts towards the Ge substrate peak (see Fig. 3) and the Sn content decreases. The $Ge_{1-x}Sn_x$ peak shift is also accompanied by broadening of the peak and disappearance of the thickness fringes, indicating degradation of crystalline quality. The surface becomes rougher, with the RMS roughness increased to 8.77 nm (Fig. 5). Islands appears on the surface with a diameter of ~300 nm and a height of ~30 nm (relative to the surface), which should arise from the Ga and Sn segregation to the surface during growth.

The impacts on the crystalline quality and the substitutionality of Sn in $Ge_{1-x}Sn_x$ arising from the change in the doped Ga concentration were also examined by RBS random and channelled spectrum. Typical RBS spectra with random and channelled alignments of the $Ge_{1-x}Sn_x$ alloys with Ga concentration of 2.1×10^{20} cm^{-3} and above 5.6×10^{20} cm^{-3} are shown in Fig. 6. Samples were mounted onto a precision 4-axis goniometer within the scattering chamber maintained at $<5\times10^{-6}$ mbar. A collimated beam of 2 MeV He^+ ions generated using the 3.5 MV Singletron accelerator at the Centre for Ion Beam Applications (CIBA) [37] was incident onto the samples. Ions backscattered at 116º were measured by a passivated implanted planar silicon (PIPS) detector, initially with the incident beam aligned with the <100> axis and subsequently close-to-random direction a few degrees off the <100> axis.

From the random spectra, the total Sn depth profile was determined using the SIMNRA simulation code,[38] and found to be flat at ~8.2% for Ga concentration of up to 2.1×10^{20} cm^{-3}, consistent with the XRD and SIMS results. The crystalline quality can be assessed by the minimum yield χ_{min}, which is the ratio of the backscattered He^+ integrated intensity in channelled alignment, to the random integrated intensity in the same region. As outermost atoms are always visible to the beam, the surface peaks in the channeled curves exist. The χ_{min} was extracted at a region just below the surface peak. The χ_{min} closely correlates with crystalline quality.[39] The measured χ_{min} values of Ge increased from 4.4% to 4.9%, with the Ga concentration increased from 8.0×10^{17} to above

5.6×10^{20} cm^{-3}. The χ_{min} values of Ge were close to that obtained from bulk Ge (3.9%), which indicates excellent crystalline quality of the $Ge_{1-x}Sn_x$ films below surface. The χ_{min} of Sn increased from 4.6% to 6.5%, which is only slightly higher than that of Ge indicating a high amount of substitutionality of Sn in the host Ge lattice. The percentage (*S*) Sn atoms located on substitutional lattice sites was calculated using the equation [39]

$$S = \frac{(1-\chi_{\min-impurity/Sn})}{(1-\chi_{\min-host/Ge})}\times 100\%. \quad (1)$$

For all samples, more than 98% of the Sn was substitutional. As the Ga composition increased, the value of χ_{min} increased, and the values of *S* tended to decrease, which may be due to the interaction between Ga and Sn atoms, or due to the crystal defects.

Spectroscopic ellipsometry measurements were carried out to evaluate the resistivity and carrier concentration of the *in-situ* Ga doped $Ge_{1-x}Sn_x$ samples. The measurements were performed at two angles of incidence (65° and 75°). The $Ge_{1-x}Sn_x$ samples were modelled as a three layer system consisting of a Ge substrate, a $Ge_{1-x}Sn_x$ film layer, and a surface layer. The dielectric function of Ge substrate was measured separately and used in tabulated form. The surface layer was modelled as a thin film consisting of 50% $Ge_{1-x}Sn_x$ and 50% voids in the Bruggeman approximation.[40] The dielectric function of the $Ge_{1-x}Sn_x$ alloy was described using an optical dispersion model, which accounts for intervalence band absorption in addition to free carrier absorption.[41] The infrared dielectric function of $Ge_{1-x}Sn_x$ alloys with various Ga doping concentrations is shown in Fig. 7. As indicated by ε_2, the free carrier absorption represented by a Drude oscillator increases with increase in Ga concentration in the alloys. The Drude model gives the electrical resistivity (ρ) and the carrier relaxation time (τ).[41,42]

The resistivity of the $Ge_{1-x}Sn_x$ samples with various Ga concentrations was also measured by micro four-point probe method, and the results are very close to that obtained by spectroscopic ellipsometry as shown in Fig. 8. The resistivity ρ is expressed as

$$\rho = \frac{1}{ne\mu}, \mu = \frac{e\tau}{m^*}, \quad (2)$$

where n is the carrier concentration, μ is the carrier mobility and m^* is the carrier effective mass in the $Ge_{1-x}Sn_x$ film. Thus the doping level can be obtained if independent measurements of m^* are available. Based on the simulation results,[43,44] we assumed that the effective mass of the alloy is $m^* = (0.20\pm0.01)m_0$ for all the Ga doped $Ge_{1-x}Sn_x$ samples, then the carrier concentration in the samples can be extracted (Fig. 7). The electrically active Ga concentrations in the $Ge_{0.915}Sn_{0.085}$ samples grown using $T_{Ga\text{-}cell}$ of 540, 640, and 740, and 820 °C are $(7.4\pm0.3)\times10^{17}$, $(1.3\pm0.1)\times10^{19}$, $(1.2\pm0.1)\times10^{20}$ and $(3.2\pm0.2)\times10^{20}$ cm^{-3}, respectively. For the $Ge_{1-x}Sn_x$ sample with Ga concentration higher than 5.6×10^{20} cm^{-3}, the electrically active Ga concentration is $(3.2\pm0.2)\times10^{20}$ cm^{-3}, excess Ga atoms cannot be incorporated, and segregate towards the surface. Figure 9 shows the electrical resistivity of p-type $Ge_{1-x}Sn_x$ alloys as a function of the carrier concentration. The results for bulk Ge, *in-situ* boron-doped $Ge_{1-x}Sn_x$ by CVD, and *in-situ* Ga-doped $Ge_{1-x}Sn_x$ by MBE are also included.[33,41,45,46] The resistivity values of $Ge_{1-x}Sn_x$ samples follow the trend, but are slightly higher than those of p-type Ge bulk materials. These results suggest degradation of mobility in p-type $Ge_{1-x}Sn_x$ alloys, which is likely due to alloy scattering in the Ge-Sn system, or due to the crystal defects. With the p-type concentration increased to ~10^{20} cm^{-3} or above, the ionized impurity scattering becomes severe, and the resistivity of $Ge_{1-x}Sn_x$ alloys becomes similar to that of Ge bulk materials.

C. $Ge_{1-x}Sn_x$/Si PIN Photodiode

To realize high-performance semiconductor devices, such as transistors, photodiodes (PDs), or lasers, low resistivity and low leakage $Ge_{1-x}Sn_x$ junctions are indispensable. $Ge_{1-x}Sn_x$ on Si PIN PDs were fabricated based on the *in-situ* Ga doping technique. Figure 10(a) shows the cross-sectional schematic of the fabricated $Ge_{0.915}Sn_{0.085}$/Si PIN photodiode. Figure 10(b) shows top view scanning electron microscopy (SEM) image of a $Ge_{0.915}Sn_{0.085}$/Si PIN photodiode having a mesa diameter (D) of 30 μm. The temperatures of all the process steps are kept below 250 °C. Figure 11(a)

This manuscript was accepted by J. Appl. Phys. Click here to see the version of record.

is the HRXRD scan of the as-grown $Ge_{0.915}Sn_{0.085}$ sample around the (004). Three separate peaks corresponding to Si substrate, Ge buffer, and $Ge_{0.95}Sn_{0.05}$ epitaxial film (from right to left) can be identified. The $Ge_{0.915}Sn_{0.085}$ film is fully strained to the Ge buffer under a biaxial compressive strain of ~1%. AFM image [Fig. 11(b)] shows that the RMS roughness of the sample was 1.73 nm (~1.6 nm before $Ge_{0.915}Sn_{0.085}$ growth). The current-voltage (*I-V*) characteristic of a $Ge_{0.915}Sn_{0.085}$/Si PIN photodiode is shown in Fig. 12(a). The diameter of the device (*D*) is 30 μm. A well-behaved $Ge_{0.915}Sn_{0.085}$/Si PIN junction was formed with a 6×10^4 on/off ratio and a low reverse current (dark current) of 0.24 μA at V_{bias} = -1 V. The dark current density is 0.034 A/cm^2 at V_{bias} = -1 V, which is the lowest value that has been reported for $Ge_{1-x}Sn_x$/Si PIN photodiodes.[47] This indicates the effectiveness of the *in-situ* Ga doping technique by MBE and the high quality of the materials grown. In order to gain additional insight into the dark current, an activation energy analysis of the $Ge_{0.915}Sn_{0.085}$/Si photodiode (*D* = 30 μm) has been performed. The I_{dark} can be modeled using

$$I_{dark} = BT^{3/2}e^{-E_a/kT}(e^{qV_a/2kT}-1) \quad (3)$$

where *B* is a constant, *T* is the temperature, E_a is the activation energy and V_a is the applied voltage. Fig. 12(b) shows the logarithm of the measured dark current $\ln(I_{dark}/T^{3/2})$ as a function of $1/kT$ for the photodiode biased at -1 V. The extracted E_a is 0.25 eV, which is around half of the bandgap (E_g) of the strained $Ge_{0.915}Sn_{0.085}$ on Ge (E_g = 0.52 eV).[48] A high density of threading dislocations through the Ge buffer and $Ge_{0.915}Sn_{0.085}$ epitaxial layer is expected due to the large lattice mismatch between Ge and Si.[10,47] Therefore, the obtained E_a of the photodiode should be associated with the threading dislocations at the bulk region.[49,50] Further investigation is needed to clarify the impact of threading dislocation on the dark current in $Ge_{1-x}Sn_x$ photodiodes.

The photoresponse characteristics of the $Ge_{0.915}Sn_{0.085}$/Si PIN photodiode were studied. The light source comprises one tunable laser with the λ from 1510 to 1630 nm, and three separate distributed feedback (DFB) laser diodes at 1742, 1877, and 2003 nm. The total current I_{total}-V_{bias} characteristic of the $Ge_{0.915}Sn_{0.085}$/Si PIN photodiode (*D* = 30 μm) under illumination is shown in Fig.

12(a). The incident light power is fixed at 0.25 mW. Obvious optical response of the $Ge_{0.915}Sn_{0.085}$/Si PIN photodiode to the light signals beyond 2 μm is observed, even at zero bias. When λ is smaller than 1600 nm, parts of the I_{photo} comes from the buffer layer since Ge also absorbs photons within this wavelength range. For λ > 1600 nm, the absorption coefficient of Ge is small even with tensile strain, and the I_{photo} should mainly come from the $Ge_{0.915}Sn_{0.085}$ layer.

IV. CONCLUSION

Heavily p-type doped $Ge_{1-x}Sn_x$ was realized by *in-situ* Ga doping at low molecular beam epitaxy temperature of 150 °C. An active doping concentration as high as ~3.2×10^{20} cm^{-3} was achieved. The dependence of crystallinity and mobility on the active Ga concentrations was investigated. High crystalline quality p-type $Ge_{0.915}Sn_{0.085}$ can be realized for active Ga concentration of up to ~1.2×10^{20} cm^{-3}. The *S* for substitutional Sn on lattice sites is higher than 98% in all p-type $Ge_{1-x}Sn_x$ samples, although it decreases as the Ga concentration increases. When the Ga concentration introduced is higher than ~3.2×10^{20} cm^{-3}, extra Ga atoms cannot be substitutionally incorporated and segregate towards the surface, accompanied by reduced Sn content in the GeSn layer as well as a degraded crystalline quality. By integrating p-type $Ge_{0.915}Sn_{0.085}$ with active Ga doping of ~1.2×10^{20} cm^{-3} in a $Ge_{0.915}Sn_{0.085}$-on-Si PIN photodiode fabrication flow, a well-behaved PIN junction was formed with a forward-bias current to reverse-bias current ratio of 6×10^4 and a low reverse current (dark current) of 0.24 μA at V_{bias} = -1 V. This indicates the effectiveness of the *in-situ* Ga doping technique by MBE and the high quality of the materials grown.

Acknowledgement

This work was supported by Singapore National Research Foundation through the Competitive Research Program (Grant No: NRF-CRP6-2010-4), the Academic Research Fund (Grant No: R-144-000-335-112), and Trailblazer Grant (R-263-000-B43-733). We acknowledge assistance from Q. Zhou on TEM analysis.

References

1. P. Guo, G. Han, X. Gong, B. Liu, Y. Yang, W. Wang, Q. Zhou, J. Pan, Z. Zhang, E. S. Tok, and Y.-C. Yeo, J. Appl. Phys. 114, 044510 (2013).
2. Y. Yang, K. L. Low, W. Wang, P. Guo, L. Wang, G. Han, and Y.-C. Yeo, J. Appl. Phys. 113, 194507 (2013).
3. X. Gong, G. Han, F. Bai, S. Su, P. Guo, Y. Yang, R. Cheng, D. Zhang, G. Zhang, C. Xue, B. Cheng, J. Pan, Z. Zhang, E. S. Tok, D. Antoniadis, and Y.-C. Yeo, IEEE Elect. Dev. Lett. 34, 339 (2013).
4. R. R. Lieten, T. Maeda, W. Jevasuwan, H. Hattori, N. Uchida, S. Miura, M. Tanaka, J. Locquet, Appl. Phys. Express, 6, 101301 (2013).
5. J. Mathews, R. Roucka, J. Xie, S. Q. Yu, J. Menendez, and J. Kouvetakis, Appl. Phys. Lett. 95, 133506 (2009).
6. J. Werner, M. Oehme, M. Schmid, M. Kaschel, A. Schirmer, E. Kasper and J. Schulze, Appl. Phys. Lett. 98, 061108 (2011).
7. D. Zhang, C. Xue, B. Cheng, S. Su, Z. Liu, X. Zhang, G. Zhang, C. Li, and Q. Wang, Appl. Phys. Lett. 102, 141111 (2013).
8. H. H. Tseng, H. Li, V. Mashanov, Y. J. Yang, H. H. Cheng, G. E. Chang, R. A. Soref, and G. Sun, Appl. Phys. Lett. 103, 231907 (2013).
9. M. Oehme, K. Kostecki, K. Ye, S. Bechler, K. Ulbricht, M. Schmid, M. Kaschel, M. Gollhofer, R. Korner, W. Zhang, E. Kasper, and J. Schulze, Optics Express 22, 839 (2014).
10. Y. Dong, W. Wang, X. Xu, X. Gong, D. Lei, Q. Zhou, Z. Xu, W. K. Loke, S.-F. Yoon, G. Liang, and Y.-C. Yeo, IEEE Trans. Electron Devices 62, 128 (2015).
11. V. R. D'Costa, C. S. Cook, A. G. Birdwell, C. L. Littler, M. Canonico, S. Zollner, J. Kouvetakis, and J. Menendez, Phys. Rev. B 73, 125207 (2006).
12. J. D. Gallagher, C. L. Senaratne, J. Kouvetakis, and J. Menendez, Appl. Phys. Lett. 105, 142102 (2014).
13. H. Lin, R. Chen, W. Lu, Y. Huo, T. I. Kamins, and J. S. Harris, Appl. Phys. Lett. 100, 102109 (2012).
14. A. A. Tonkikh, C. Eisenschmidt, V. G. Talalaev, N. D. Zakharov, J. Schilling, G. Schmidt, and P. Werner, Appl. Phys. Lett. 103, 032106 (2013).
15. W. J. Yin, X. G. Gong, S. H. Wei, Phys. Rev. B, 78, 161203 (2008).

16. S. Wirths, Z. Ikonic, A. T. Tiedemann, B. Hollander, T. Stoica, G. Mussler, U. Breuer, J. M. Hartmann, A. Benedetti, S. Chiussi, D. Grutzmacher, S. Mantl, and D. Buca, Appl. Phys. Lett. 103, 192110 (2013).
17. S. Wirths, R. Geiger, N. von den Driesh, G. Mussler, T. Stoica, S. Mantl, Z. Ikonic, M. Luysberg, S. Chiussi, J. M. Hartmann, H. Sigg, J. Faist, D. Buca and D. Grutzmacher, Nature Photonics 9, 88(2015).
18. G. He, H. A. Atwater, Appl. Phys. Lett. 68, 664 (1996).
19. J. Kouvetakis, J. Menendez, A. V. G. Chizmeshya, Annu. Rev. Mater. Res. 36, 497 (2006).
20. S. Takeuchi, A. Sakai, K. Yamamoto, O. Nakatsuka, M. Ogawa, S. Zaima, Semicond. Sci. Technol. 22, S231 (2007).
21. N. Bhargava, M. Coppinger, J. P. Gupta, L. Wielumski, J. Kolodzey, Appl. Phys. Lett. 103, 041908 (2013).
22. A. A. Tonkikh, N. Zakharov, A. Suvorova, C. Eisenschmidt, J. Schilling, and P. Werner, Crys. Growth & Design 14, 1617 (2014).
23. W. Wang, Q. Zhou, Y. Dong, E. S. Tok, and Y. C. Yeo, Appl. Phys. Lett. 106, 232106 (2015).
24. H. Li, C. Chang, T. P. Chen, H. H. Cheng, Z. W Shi, and H. Chen, Appl. Phys. Lett. 105, 151906 (2014).
25. W. Wang, L. Li, Q. Zhou, J. S. Pan, Z. Zhang, E. S. Tok, Y. C. Yeo, Appl. Surf. Sci. 321, 240 (2014).
26. C. O. Chui, K. Gopalakrishnam, P. B. Griffin, J. D. Plummer, and K. C. Saraswat, Appl. Phys. Lett. 83, 3275 (2003).
27. Y. L. Chao, S. Prussin, J. C. S. Woo, and R. Scholz, Appl. Phys. Lett. 87, 142102 (2005).
28. M. Mirabella, G. Impellizzeri, A. M. Piro, E. Bruno, and M. G. Grimaldi, Appl. Phys. Lett. 92, 251909 (2008).
29. G. Han, S. Su, Q. Zhou, L. Wang, W. Wang, G. Zhang, C. Xue, B. Cheng, and Y. C. Yeo, International Workshop on Junction Technology, 2012, 106.
30. O. Madelung, Semiconductors: Data Handbook 3rd edition, Springer, Heidelberg, 2003.
31. G. Hellings, C. Wuendisch, G. Eneman, E. Simoen, T. Clarysse, M. Meuris, W. Vandervorst, M. Posselt, and K. De Meyer, Electrochem. Solid-State Lett. 12, H417 (2009).
32. T. Herrmannsdorfer, V. Heera, O. Ignatchik, M. Uhlarz, A. Mucklich, M. Posselt, H. Reuther, B. Schmidt, K. H. Heinig, W. Skorupa, M. Voelskow, C. Wundisch, R. Skrotzki, M. Helm, and J. Wosnitza, Phys. Rev. Lett. 102, 217003 (2009).

33. Y. Shimura, S. Takeuchi, O. Nakatsuka, B. Vincent, F. Gencarelli, T. Clarysse, W. Vandervorst, M. Caymax, R. Loo, A. Jensen, D. H. Petersen, and S. Zaima, Thin Solid Films 520, 3206 (2012).
34. Y. L. Chao and J. C. S. Woo, IEEE Trans. Electron Devices 57, 665 (2010).
35. W. Wang, L. Li, E. S. Tok, and Y. C. Yeo, J. Appl. Phys. 117, 225304 (2015).
36. J. C. Slater, J. Chem. Phys. 39, 3119 (1964).
37. F. Watt, J. A. van Kan, I. Rajta, A. A. Bettiol,T. F. Choo, M. B. H. Breese, T. Osipowicz, Nucl. Instrum. Methods Phys. Res. B 210, 14 (2003).
38. M. Mayer, SIMNRA User's Guide, Report IPP 9/113, Max-Planck-Institut für Plasmaphysik, Garching, Germany (1997).
39. L. C. Feldman, J. W. Mayer, S. T. A. Picraux, Materials Analysis by Ion Channeling: Submicron Crystallography (Academic Press, 1982).
40. C. F. Bohren and D. R. Huffman, Absorption and Scattering of Light by Small Particles (Wiley-Interscience, New York, 1983).
41. V. R. D'Costa, J. Tolle, J. Xie, J. Kouvetakis, and J. Menendez, Phys. Rev. B 80, 125209 (2009).
42. T. E. Tiwald, D. W. Thompson, J. A. Woollam, W. Paulson, and R. Hance, Thin Solid Films 313-314, 661 (1998).
43. N. Yahyaoui, N. Sfina, J. L. Lazzari, A. Bournel, and M. Said, J. Appl. Phys. 115, 033109 (2014).
44. K. L. Low, Y. Yang, G. Han, W. Fan, and Y. C. Yeo, J. Appl. Phys. 112, 103715 (2012).
45. O. A. Golikova, B. Y. Moizhez, and L. S. Stilbans, Sov. Phys. Solid State 3, 2259 (1962).
46. B. Vincent, F. Gencarelli, H. Bender, C. Merckling, B. Douhard, D. H. Petersen, O. Hansen, H. H. Henrichsen, J. Meersschaut, W. Vandervorst, M. Heyns, R. Loo, M. Caymax, Appl. Phys. Lett. 99, 152103 (2011).
47. Y. Dong, W. Wang, D. Lei, X. Gong, Q. Zhou, S. Y. Lee, W. K. Loke, S. F. Yoon, E. S. Tok, G. Liang, and Y. C. Yeo, Optics Express 23, 18611 (2015).
48. G. E. Chang, S. W. Chang and S. L. Chuang, IEEE J. Quant. Electron., 46, 1813 (2010).
49. R. N. Hall, Phys. Rev., 87, 387 (1952).
50. P. N. Grillot, S. A. Ringel, E. A. Fitzgerald, G. P. Watson, Y. H. Xie, J. Appl. Phys., 77, 3248 (1995).

List of Figures and Captions

Figure 1 (004) HRXRD curves of BF_2^+ implanted (a) $Ge_{0.975}Sn_{0.025}$ and (b) $Ge_{0.92}Sn_{0.08}$ films after RTA at various temperatures for 5 minutes. For $Ge_{0.92}Sn_{0.08}$ film, anneal cannot recover the crystallinity to the as-grown level.

Figure 2 SIMS depth profiles of (a) Ga and (b) Sn for the $Ge_{1-x}Sn_x$ films grown at fixed Ge and Sn cell temperatures to realize a nominal x of 0.085, and with the Ga cell temperature $T_{Ga\text{-}cell}$ varied to realize various *in-situ* Ga doping concentrations.

Figure 3 (004) HRXRD curves of the $Ge_{1-x}Sn_x$ samples with various Ga cell temperatures $T_{Ga\text{-}cell}$ or *in-situ* Ga doping concentrations. The Ge and Sn cell temperatures were fixed so that the nominal x is 0.085. $Ge_{1-x}Sn_x$ samples with x = 0.085 and high crystalline quality can be achieved for $T_{Ga\text{-}cell}$ of up to 740 °C or for Ga concentration of up to 2.1×10^{20} cm^{-3}.

Figure 4 (a) Cross-sectional TEM image of the $Ge_{0.915}Sn_{0.085}$ film with Ga concentration of 2.1×10^{20} cm^{-3}, achieved with $T_{Ga\text{-}cell}$ of 740 °C. HRTEM image of (b) surface region and (c) interface region between $Ge_{0.915}Sn_{0.085}$ and Ge.

Figure 5 AFM images of the $Ge_{1-x}Sn_x$ samples with Ga concentration of (a) 8.0×10^{17} cm^{-3}, (b) 1.5×10^{19} cm^{-3}, (c) 2.1×10^{20} cm^{-3} and (d) $>5.6\times10^{20}$ cm^{-3}. Smooth p $Ge_{1-x}Sn_x$ can be achieved for Ga concentration of up to 2.1×10^{20} cm^{-3}.

Figure 6 Random and aligned RBS spectra of the $Ge_{1-x}Sn_x$ samples with Ga concentration of (a) 2.1×10^{20} cm^{-3} and (b) $>5.6\times10^{20}$ cm^{-3}.

Figure 7 (a) Real and (b) imaginary parts of the infrared dielectric function of the $Ge_{0.915}Sn_{0.085}$ films with various Ga concentrations. The curves reveal strong free-carrier response.

Figure 8 The resistivity of the $Ge_{0.915}Sn_{0.085}$ films with various *in-situ* Ga doping concentration as measured by micro four-point probe and infrared ellipsometry.

Figure 9 Electrical resistivity of p-type $Ge_{1-x}Sn_x$ alloys as a function of electrically active doping concentration.

Figure 10 (a) Cross-sectional schematic of the $Ge_{0.915}Sn_{0.085}$/Si PIN photodiode having an *in-situ* Ga doped p^+ $Ge_{0.915}Sn_{0.085}$ region. (b) Top view SEM image of a PIN photodiode having a diameter of 30 μm.

Figure 11 (a) (004) HRXRD rocking curve of the p-type $Ge_{0.915}Sn_{0.085}$ on Ge/Si virtual substrate. (b) AFM image on the p^+ $Ge_{0.915}Sn_{0.085}$ surface.

Figure 12 (a) *I-V* characteristics with and without illumination of the $Ge_{0.915}Sn_{0.085}$/Si PIN photodiode. The light wavelength λ ranges from 1550 to 2003 nm. The arrow indicates the direction of increasing λ. The incident light power is fixed at 0.25 mW. (b) Plot of $\ln(I_{dark}/T^{3/2})$ *vs.* $1/kT$ for the photodiode at -1 V. The extracted E_a of the photodiode is 0.25 eV.

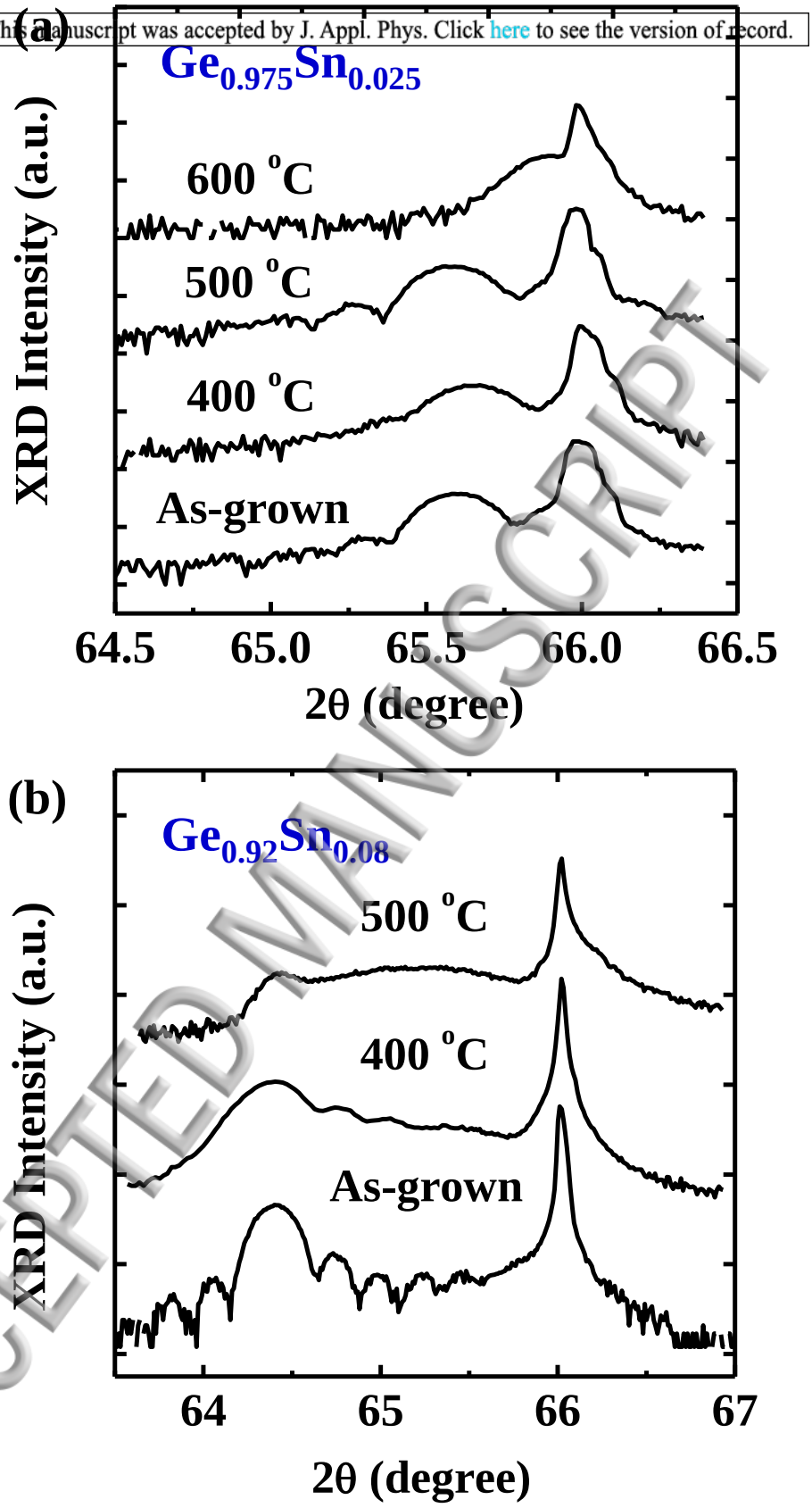

FIG. 1. Wang *et al.*

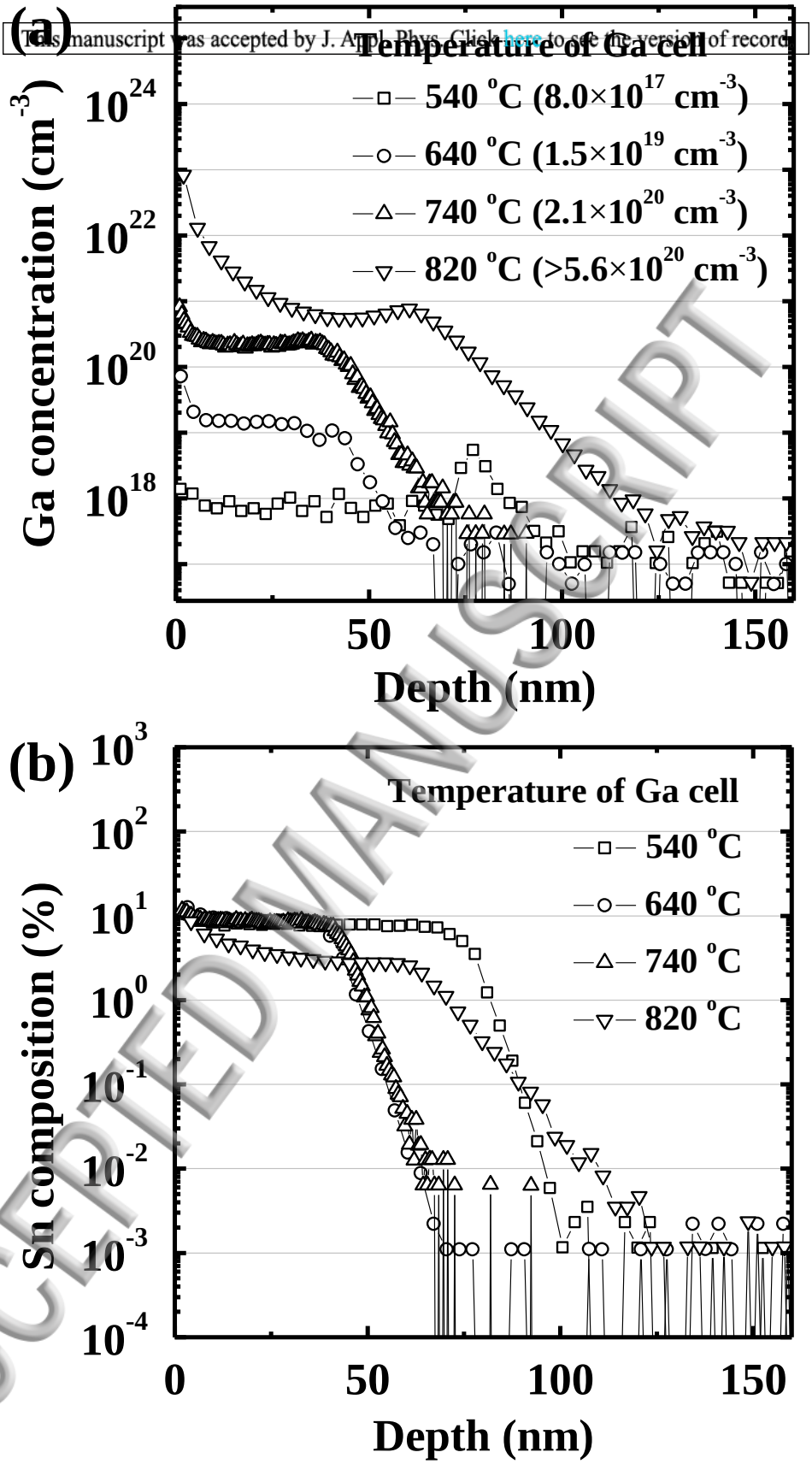

FIG. 2. Wang *et al.*

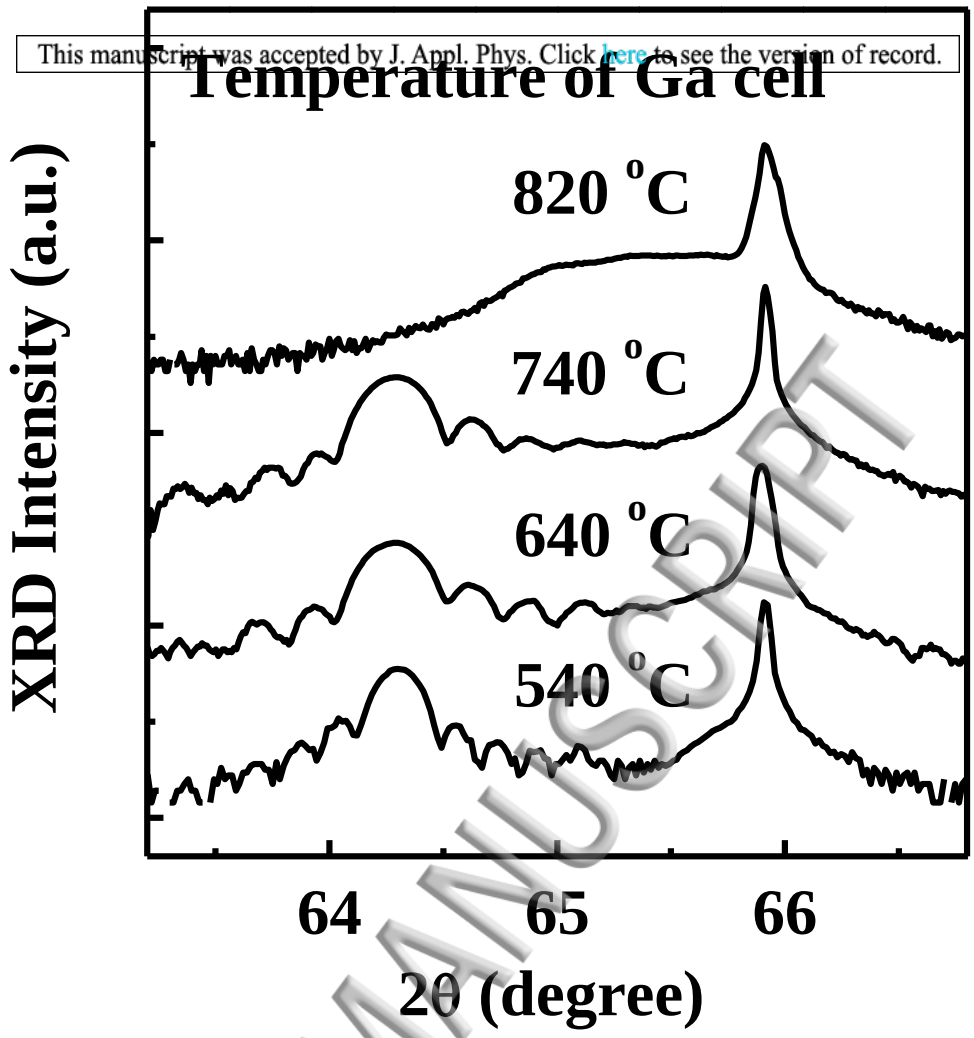

FIG. 3. Wang *et al.*

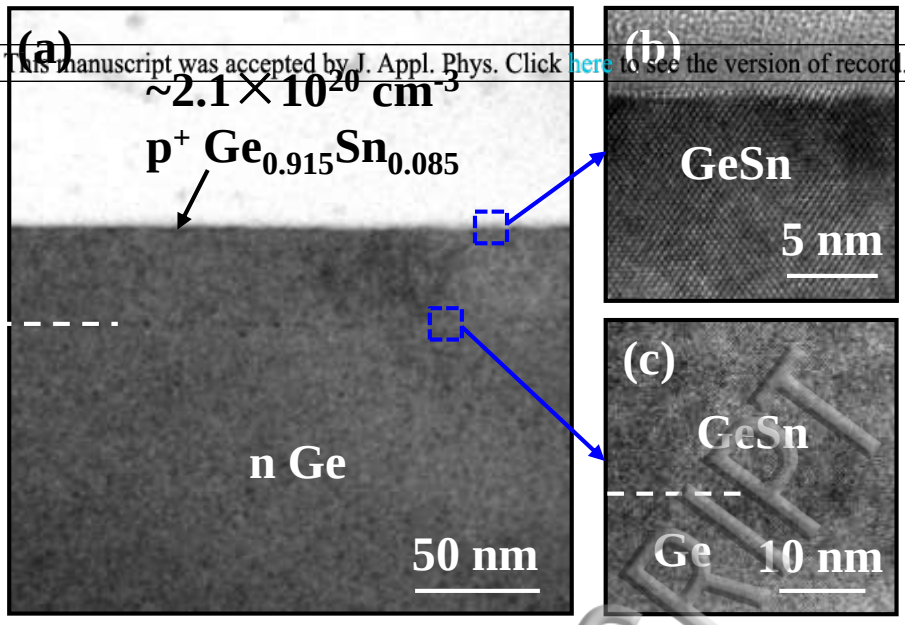

FIG. 4. Wang *et al.*

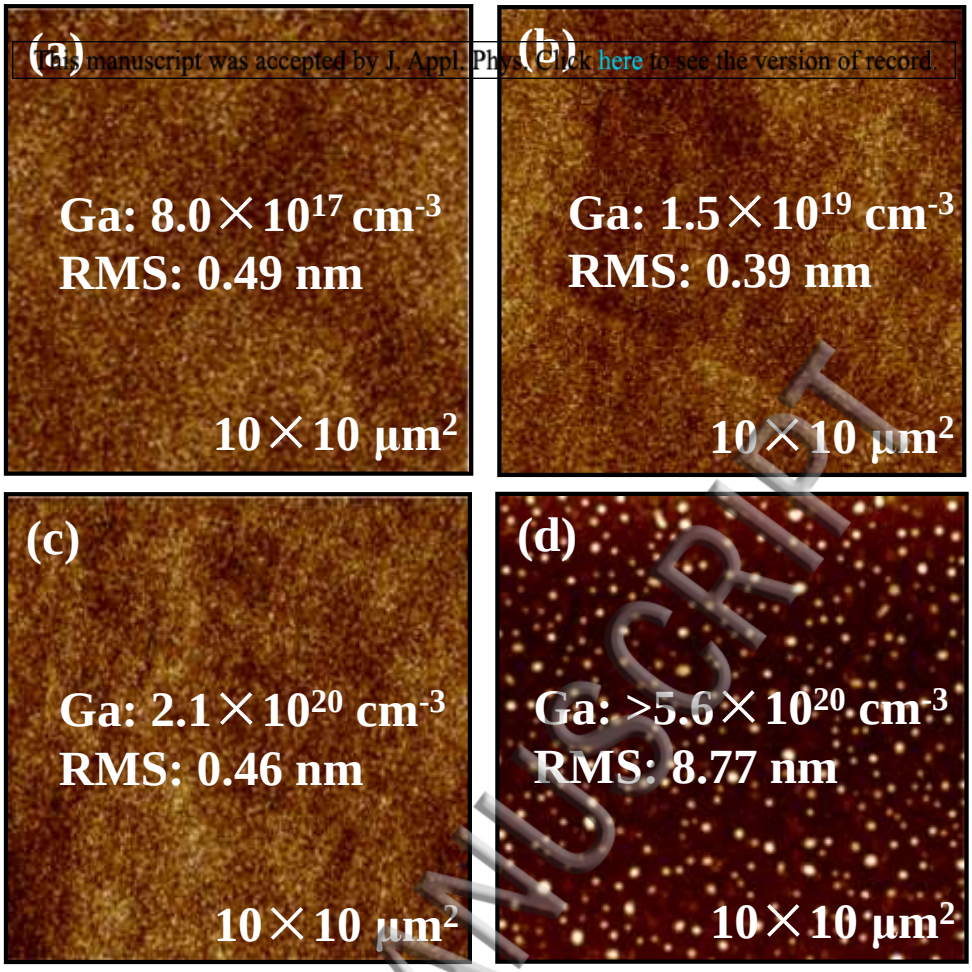

FIG. 5. Wang *et al.*

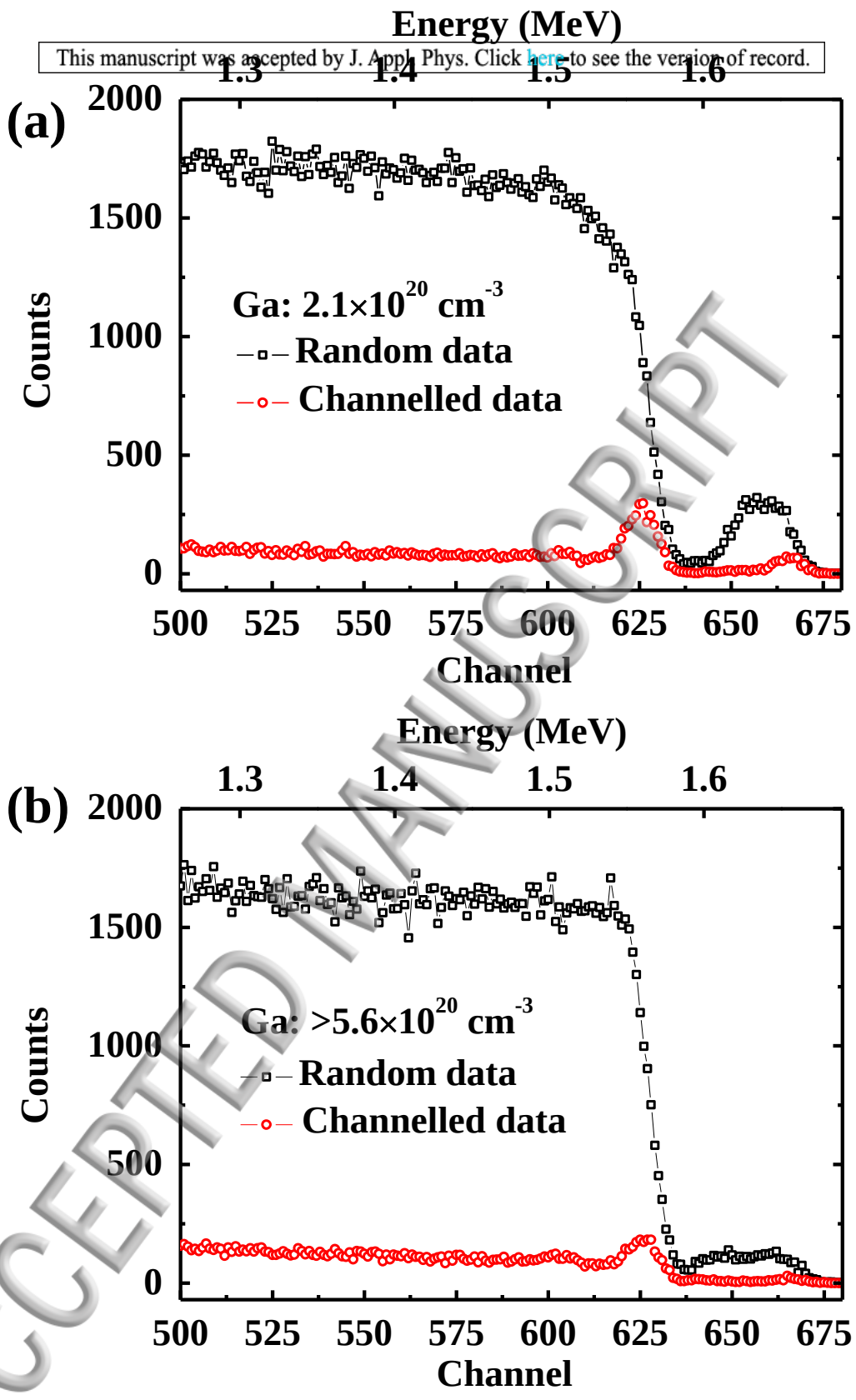

FIG. 6. Wang *et al.*

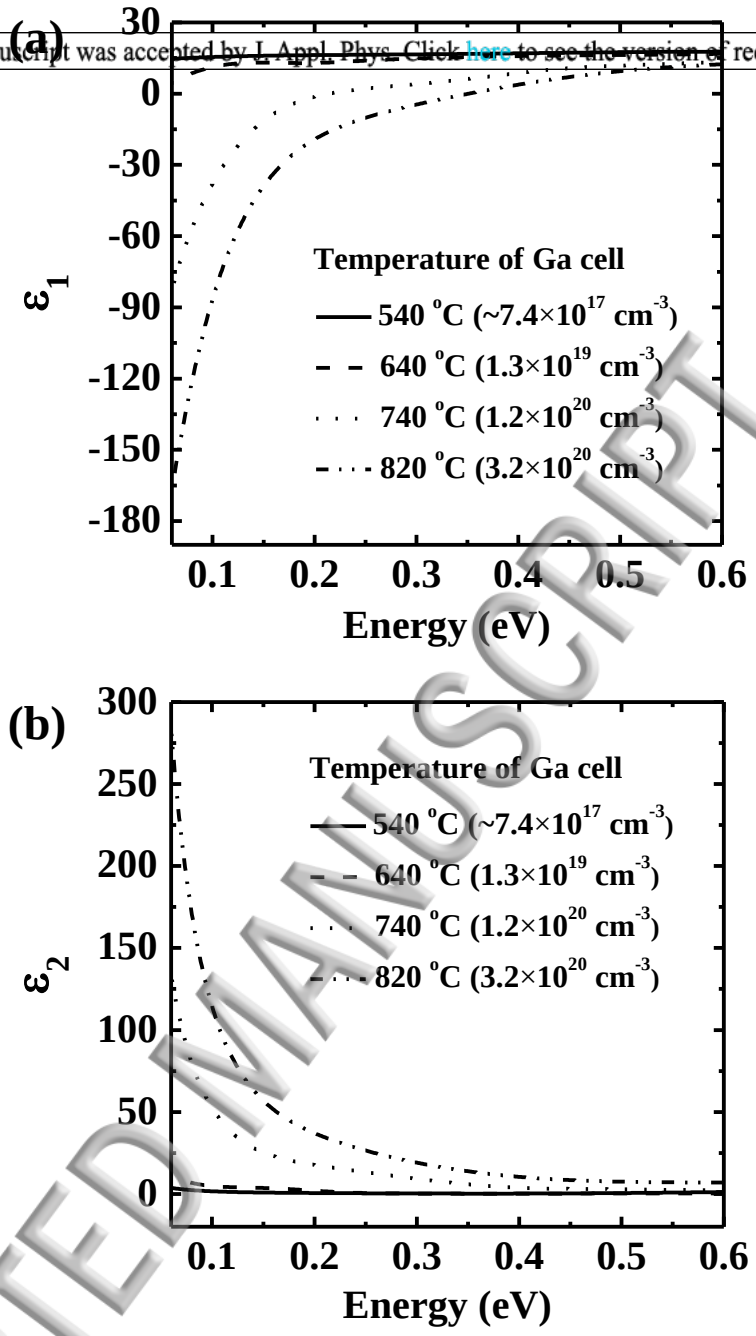

FIG. 7. Wang *et al*.

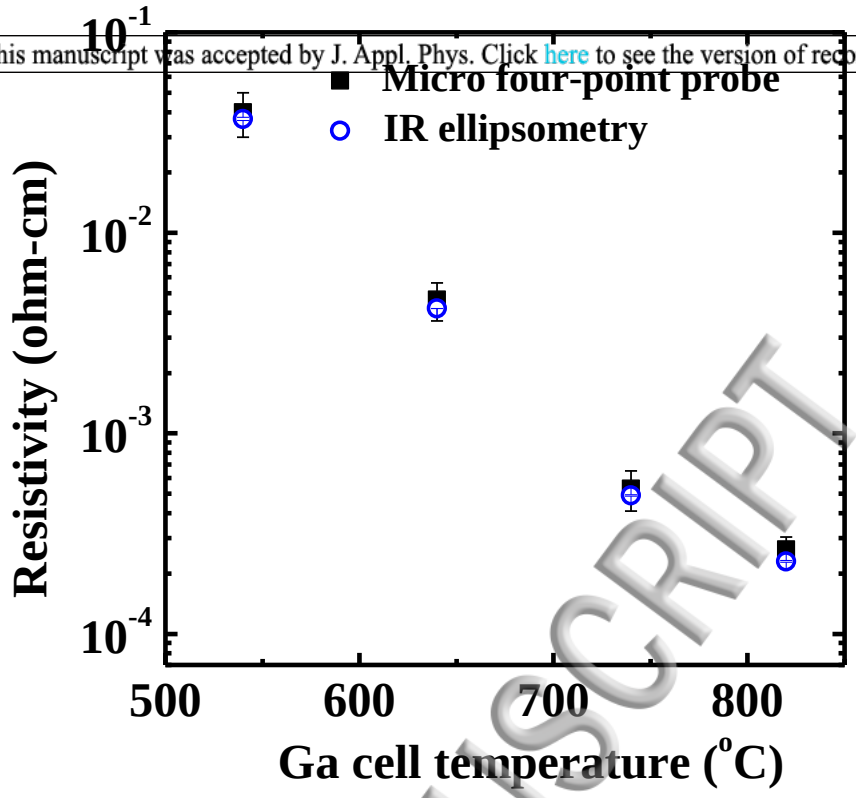

FIG. 8. Wang *et al.*

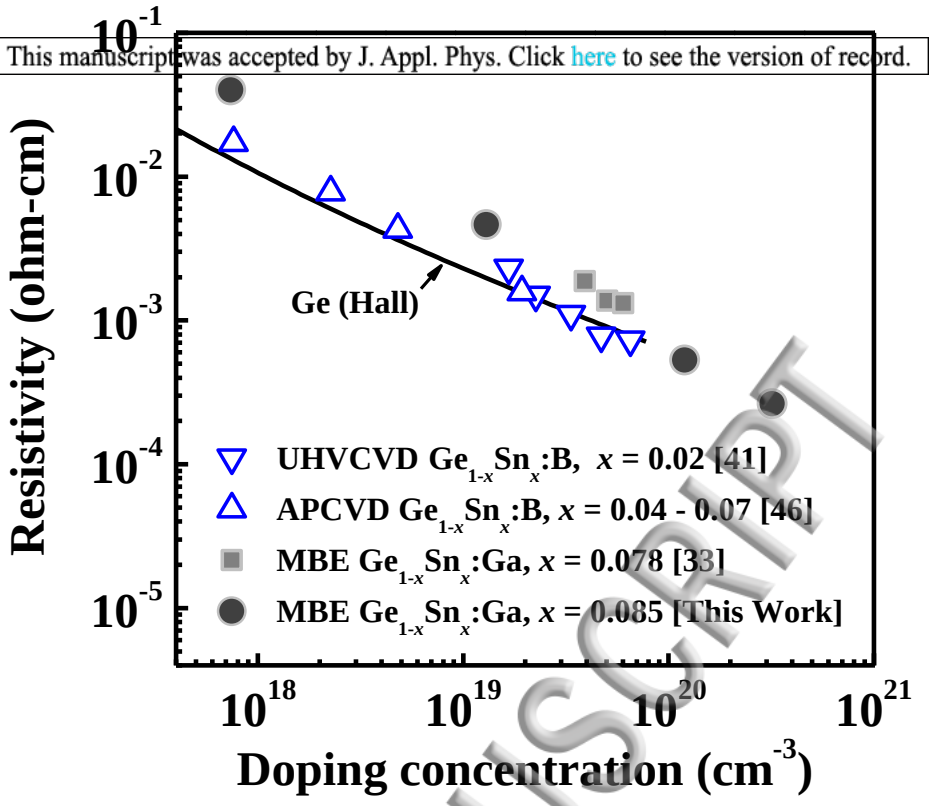

FIG. 9. Wang *et al.*

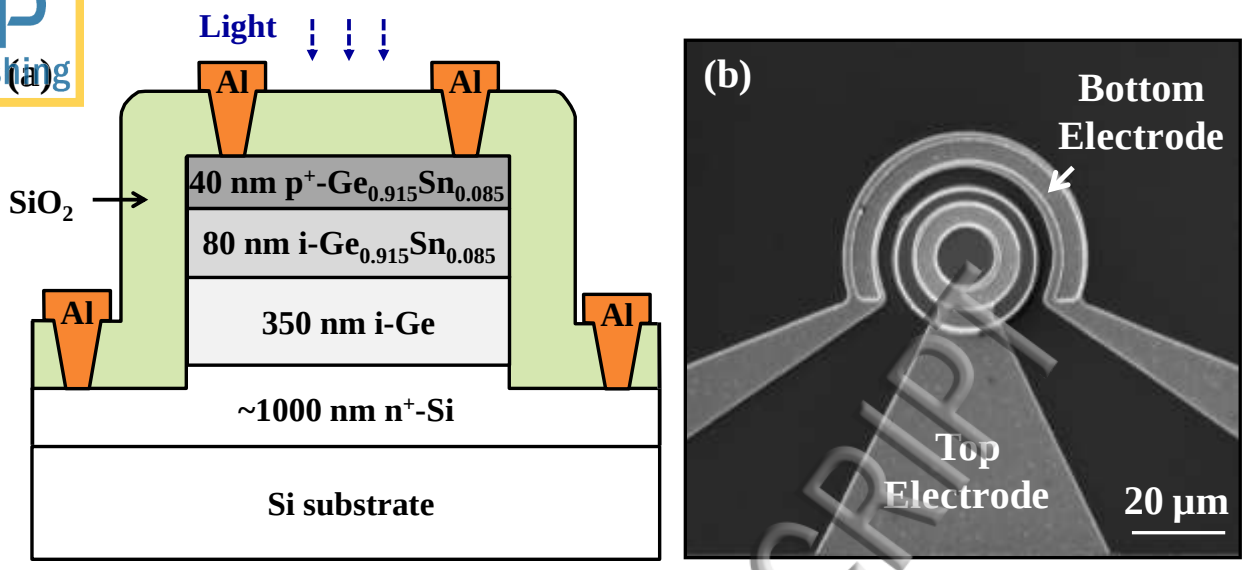

FIG. 10. Wang *et al.*

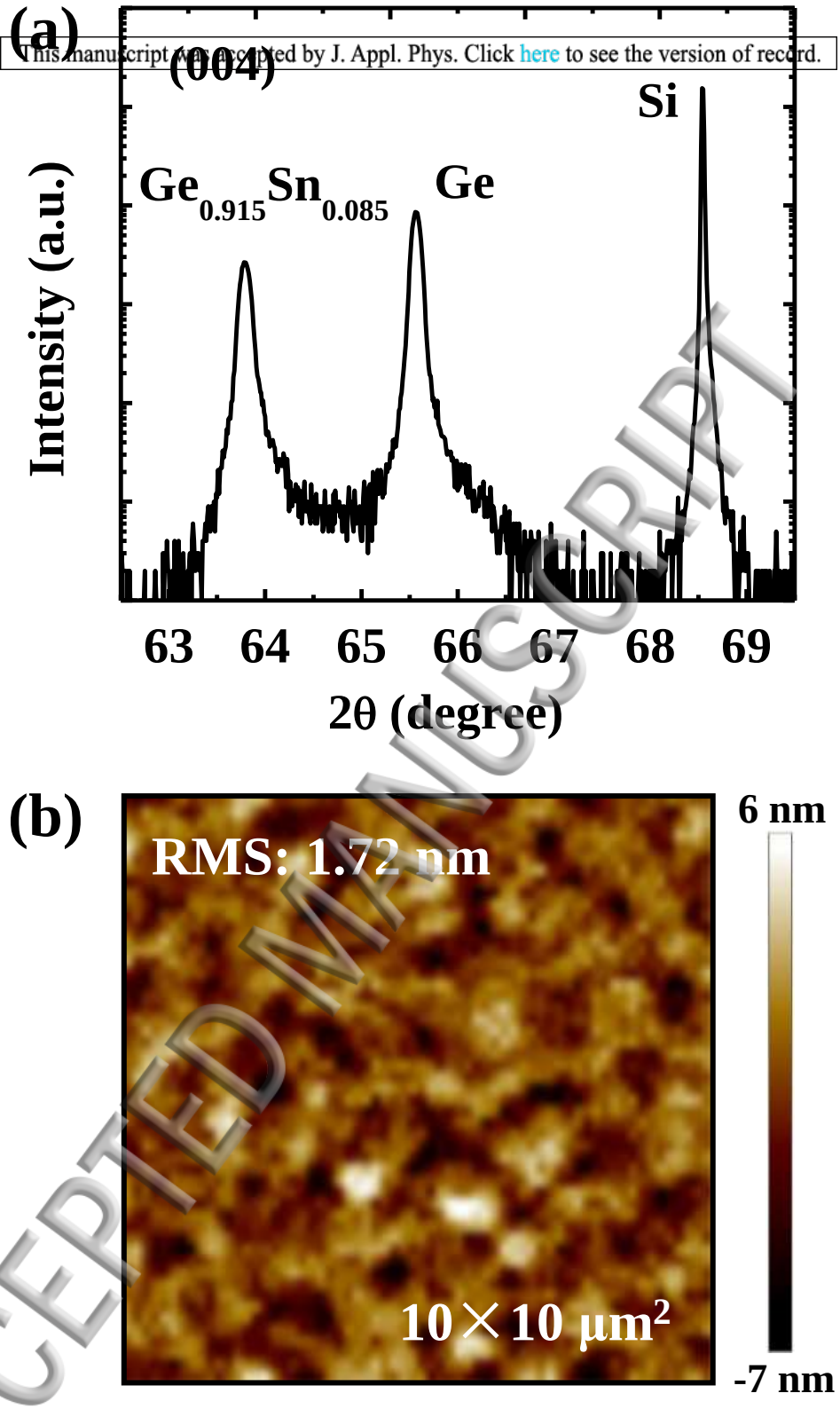

FIG. 11. Wang *et al.*

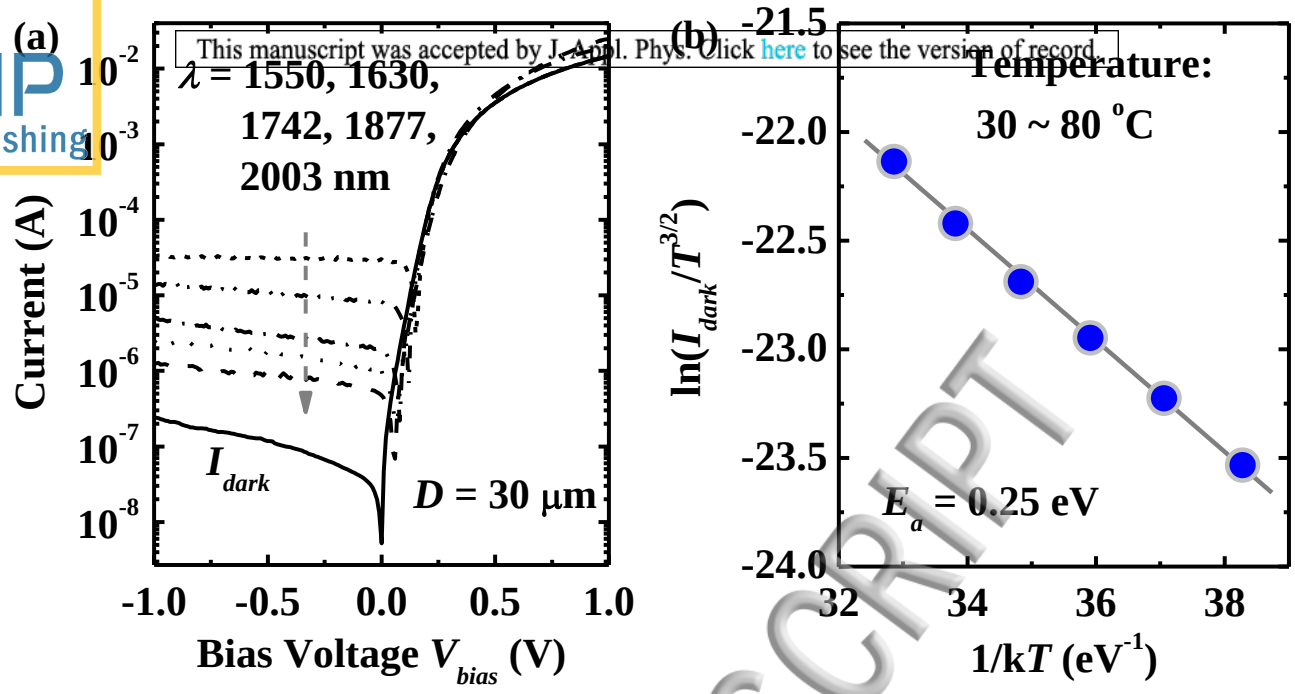

FIG. 12. Wang *et al.*

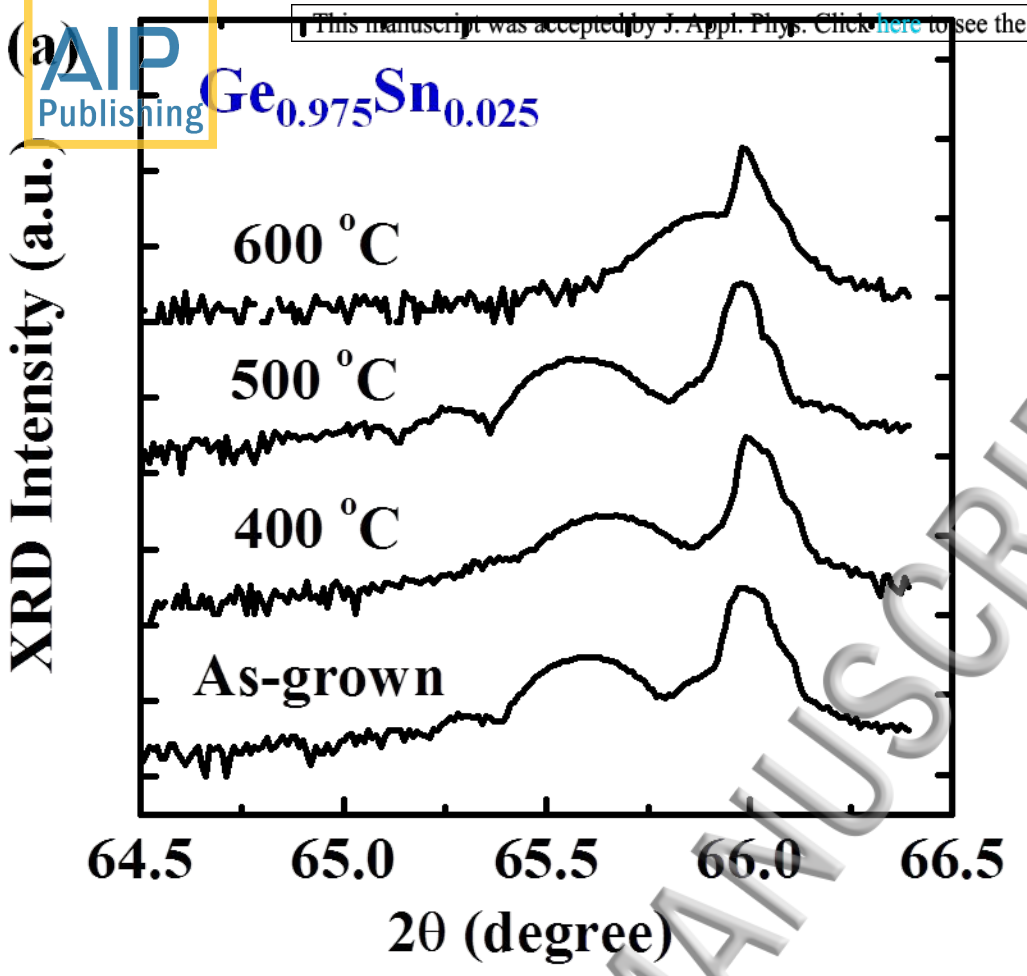

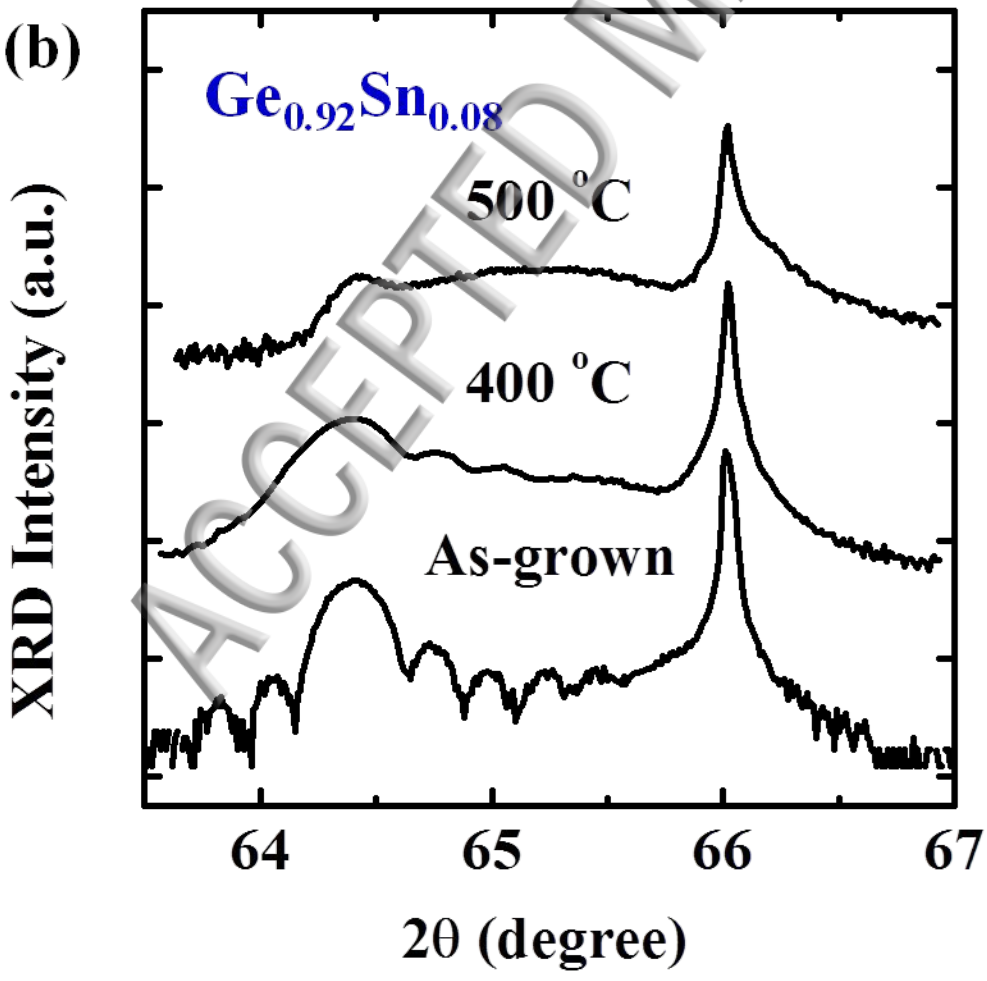

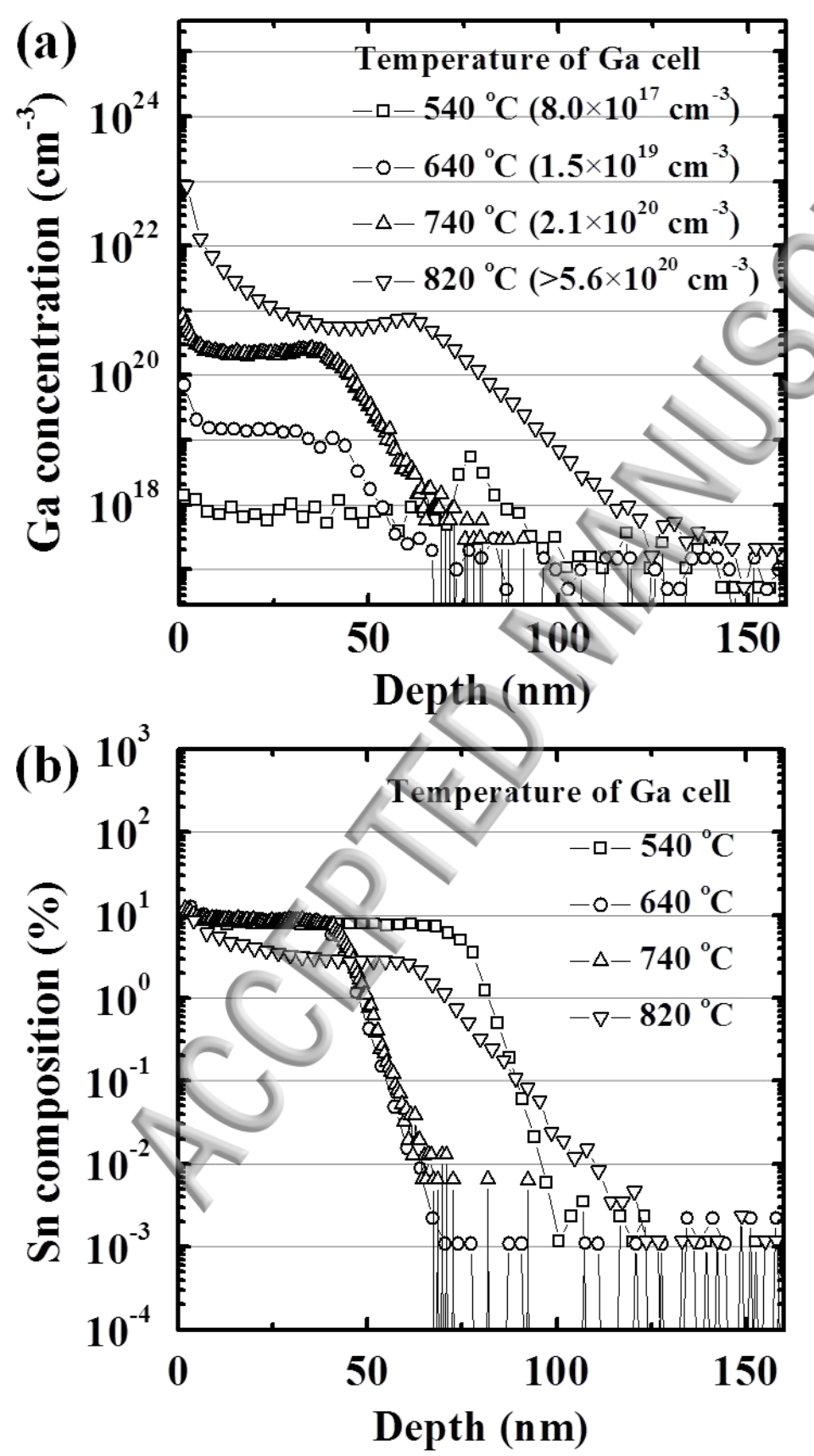

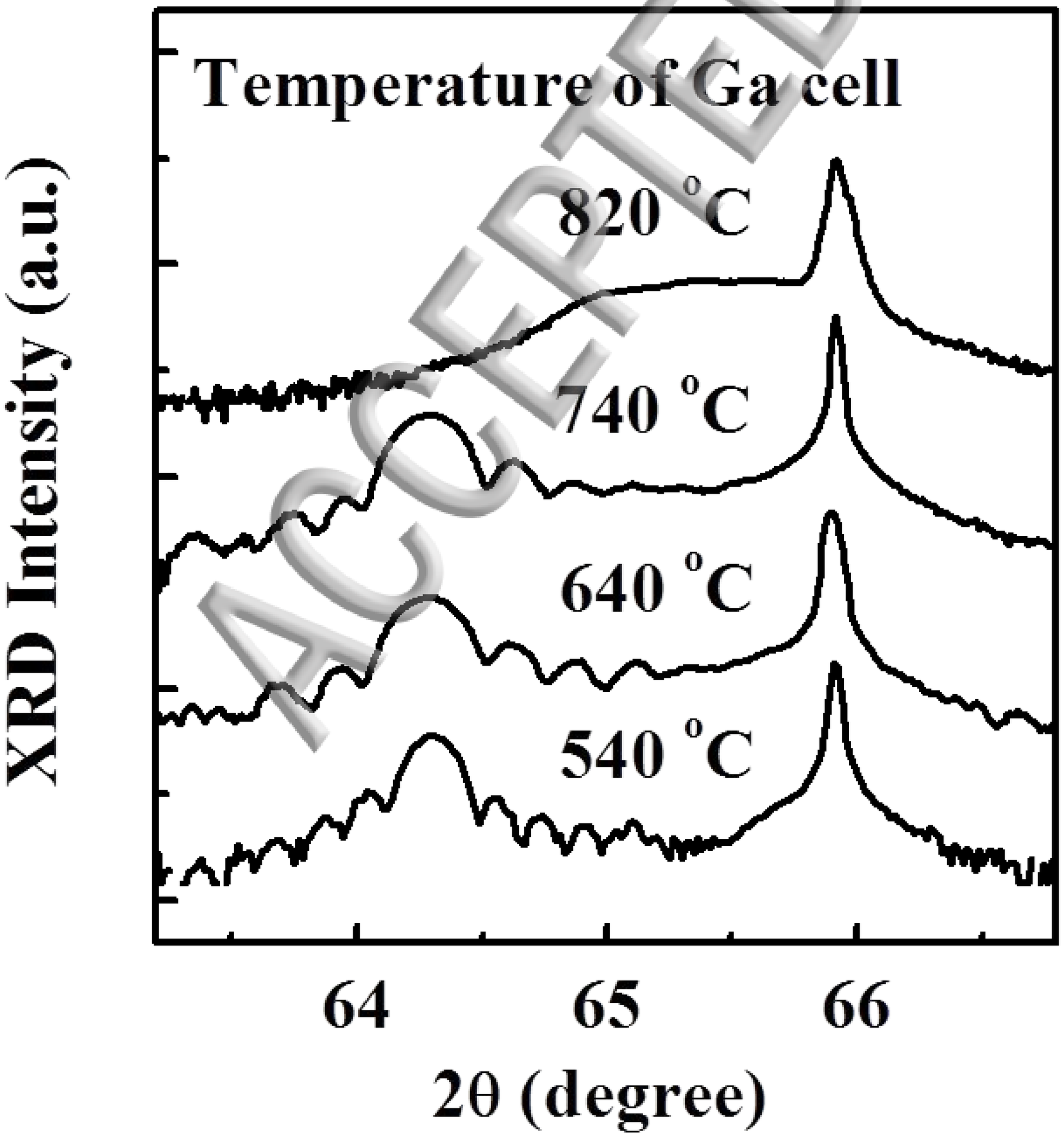
Temperature of Ga cell
820 °C
740 °C
640 °C
540 °C
XRD Intensity (a.u.)
64
65
66
2θ (degree)

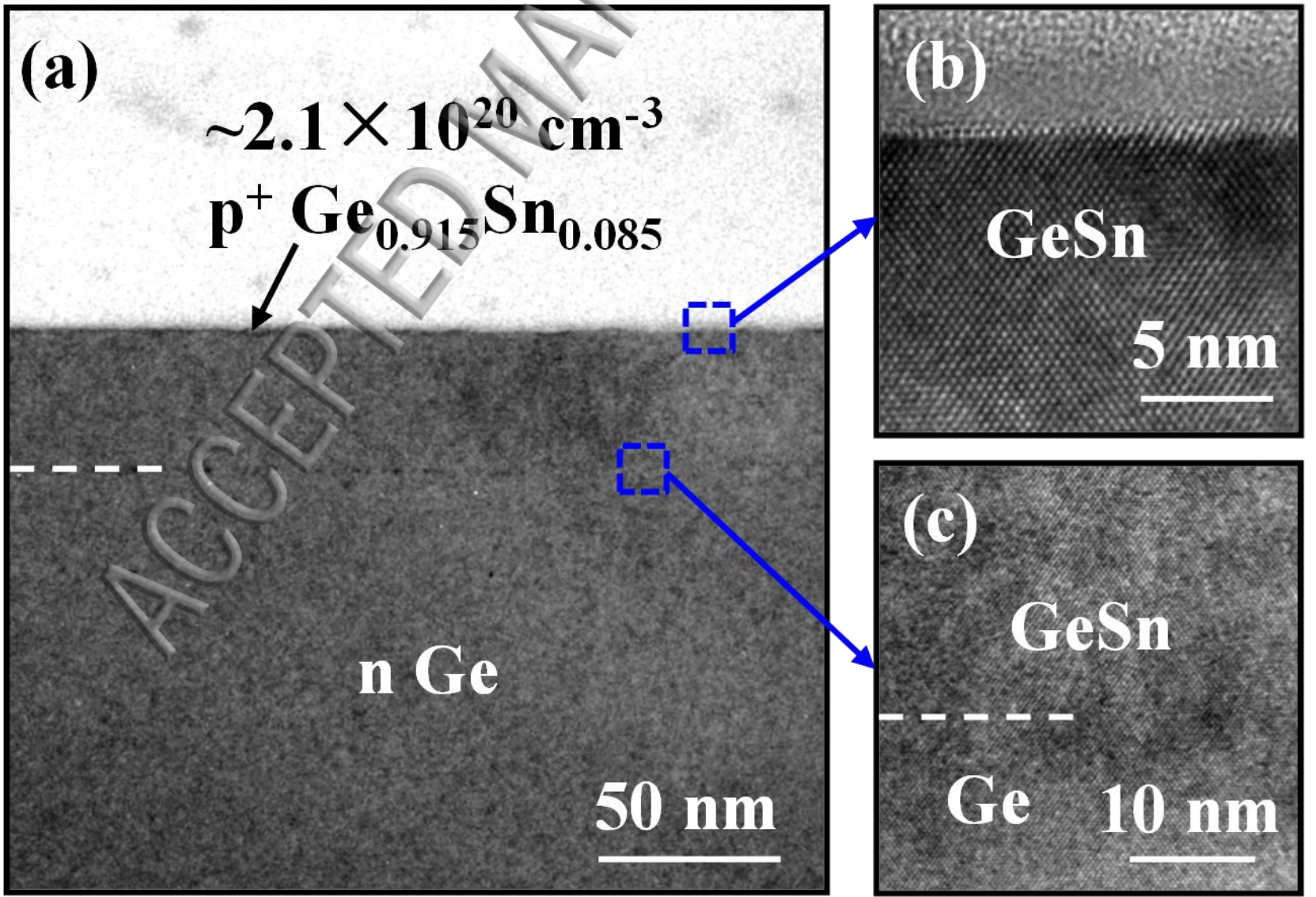

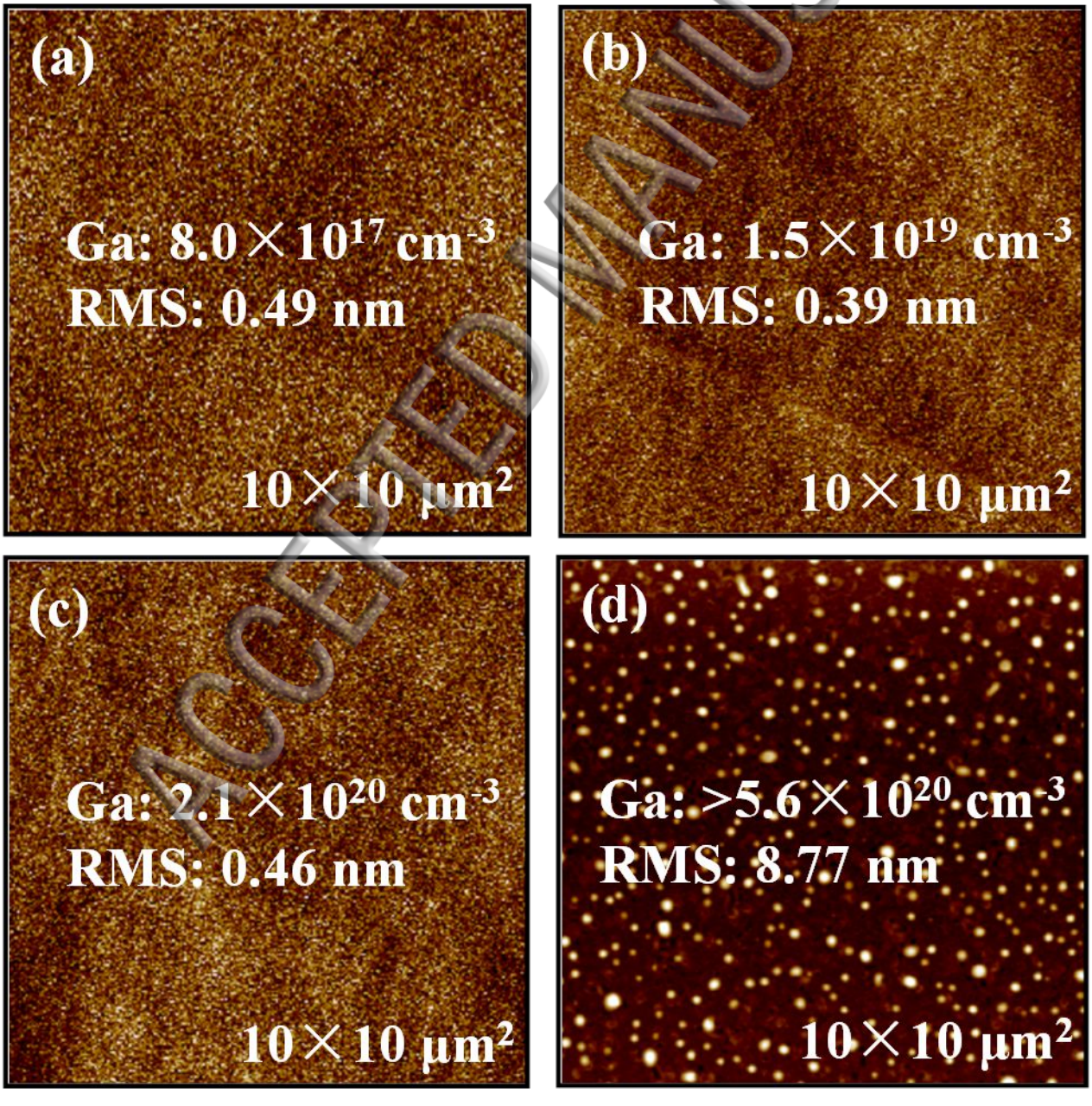

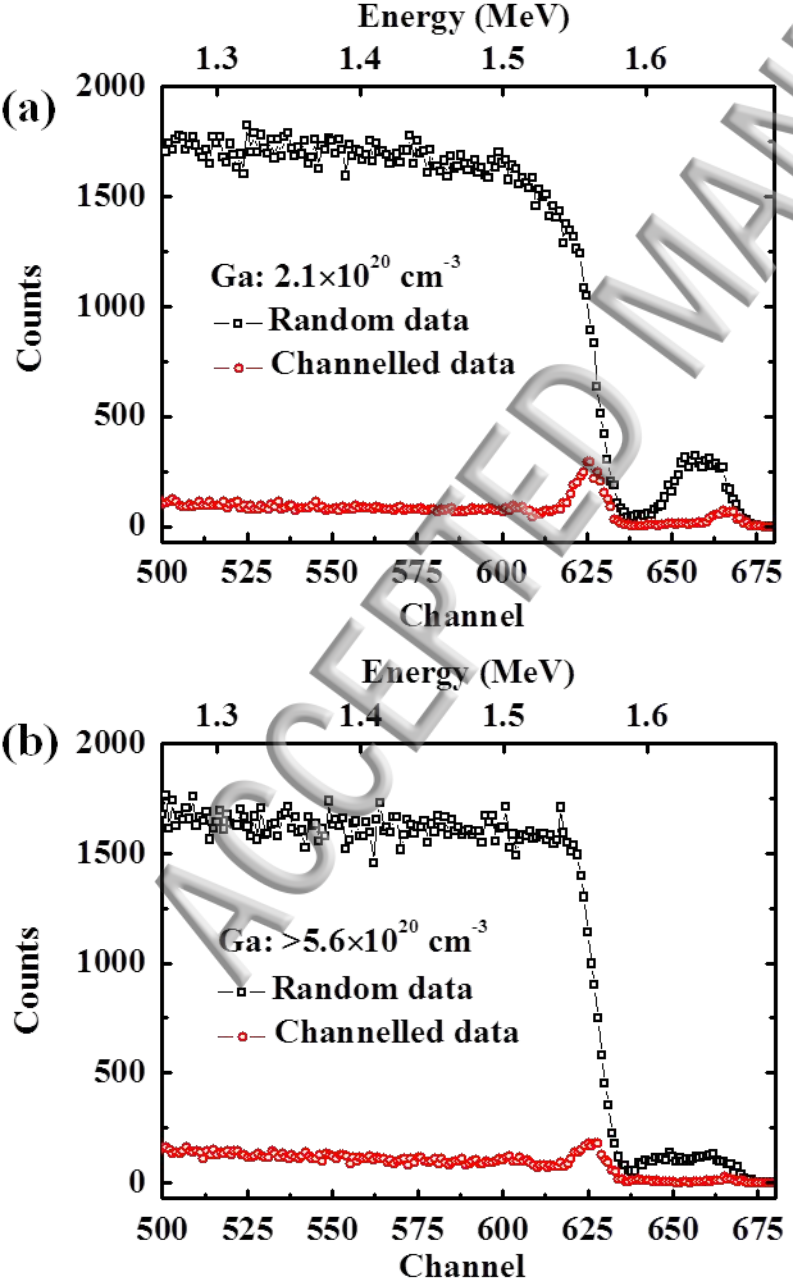

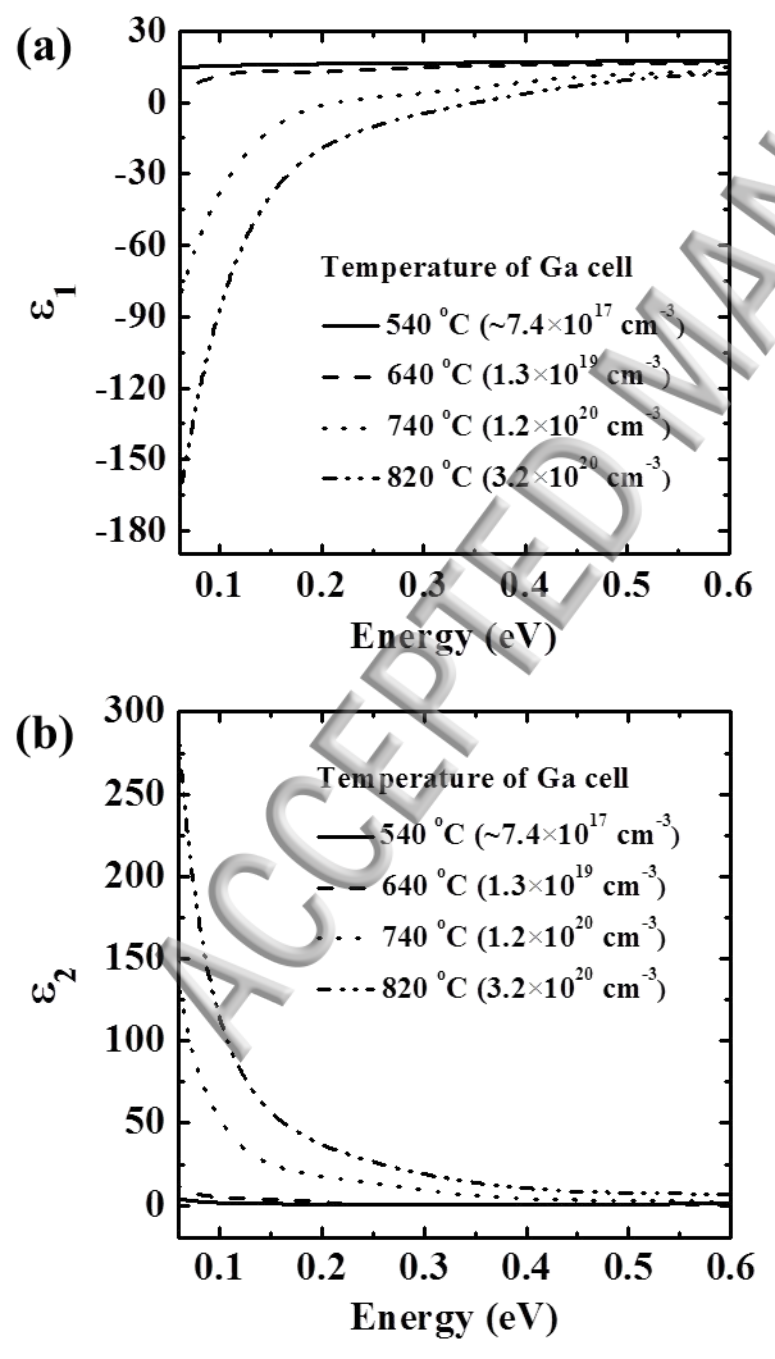
(a)
30
0
-30
-60
-90
-120
-150
-180
ε_1
Temperature of Ga cell
540 °C (~7.4×10^17 cm^-3)
640 °C (1.3×10^19 cm^-3)
740 °C (1.2×10^20 cm^-3)
820 °C (3.2×10^20 cm^-3)
0.1
0.2
0.3
0.4
0.5
0.6
Energy (eV)
(b)
300
250
200
150
100
50
0
ε_2
Temperature of Ga cell
540 °C (~7.4×10^17 cm^-3)
640 °C (1.3×10^19 cm^-3)
740 °C (1.2×10^20 cm^-3)
820 °C (3.2×10^20 cm^-3)
0.1
0.2
0.3
0.4
0.5
0.6
Energy (eV)

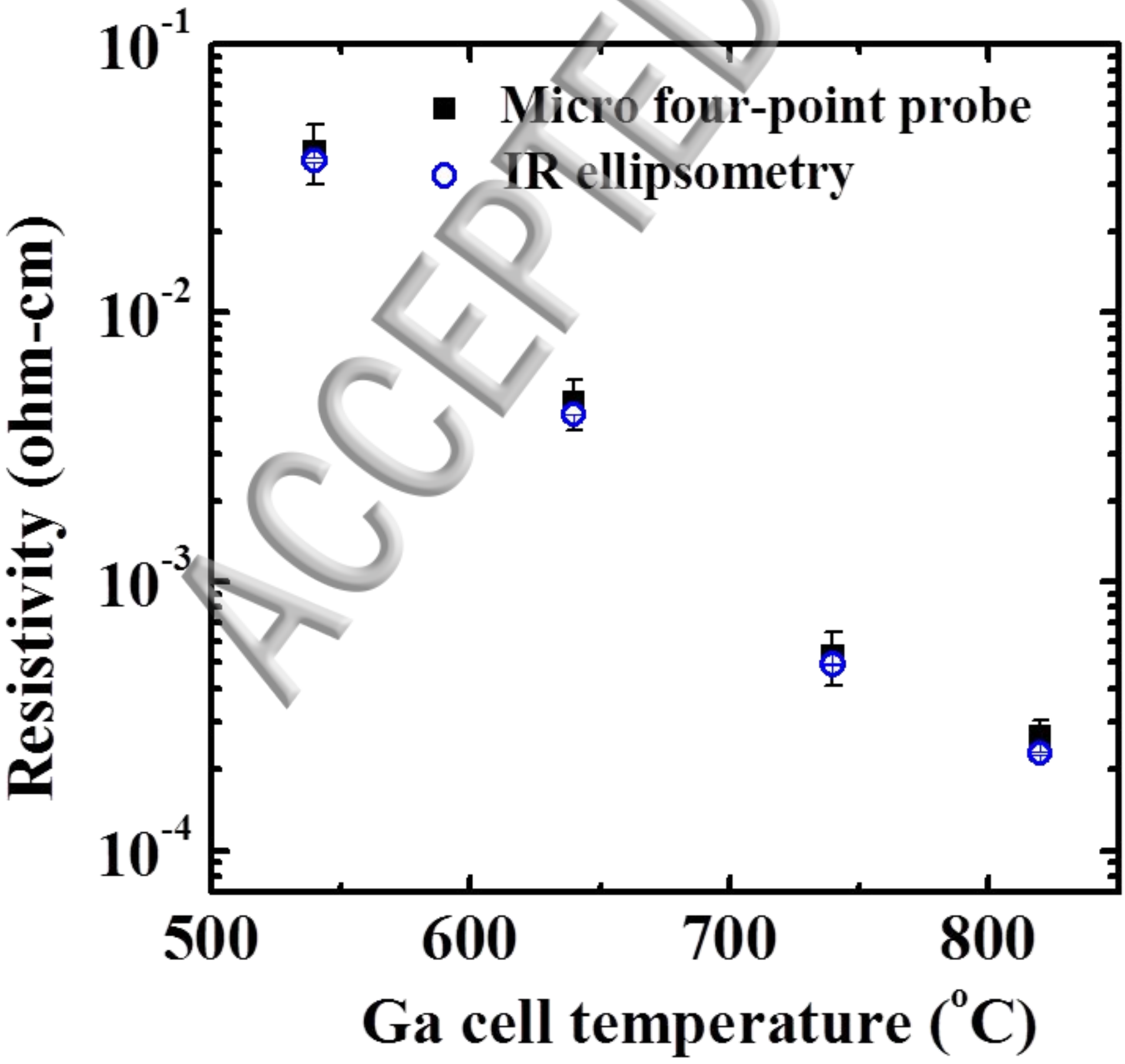
Micro four-point probe
IR ellipsometry
Resistivity (ohm-cm)
10^-1
10^-2
10^-3
10^-4
500
600
700
800
Ga cell temperature (°C)

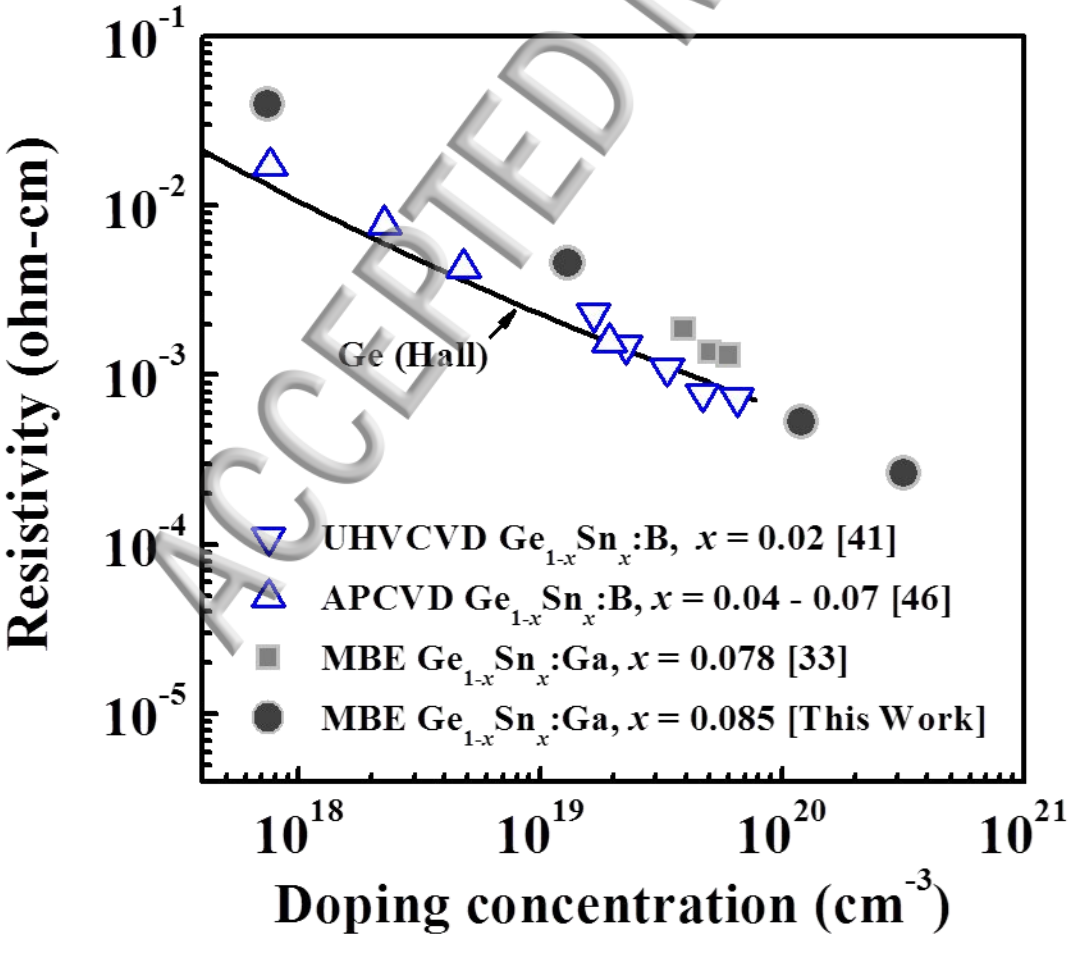
Resistivity (ohm-cm)
10^{-1}
10^{-2}
10^{-3}
10^{-4}
10^{-5}
Ge (Hall)
UHVCVD $Ge_{1-x}Sn_x$:B, x = 0.02 [41]
APCVD $Ge_{1-x}Sn_x$:B, x = 0.04 - 0.07 [46]
MBE $Ge_{1-x}Sn_x$:Ga, x = 0.078 [33]
MBE $Ge_{1-x}Sn_x$:Ga, x = 0.085 [This Work]
10^{18}
10^{19}
10^{20}
10^{21}
Doping concentration (cm^{-3})

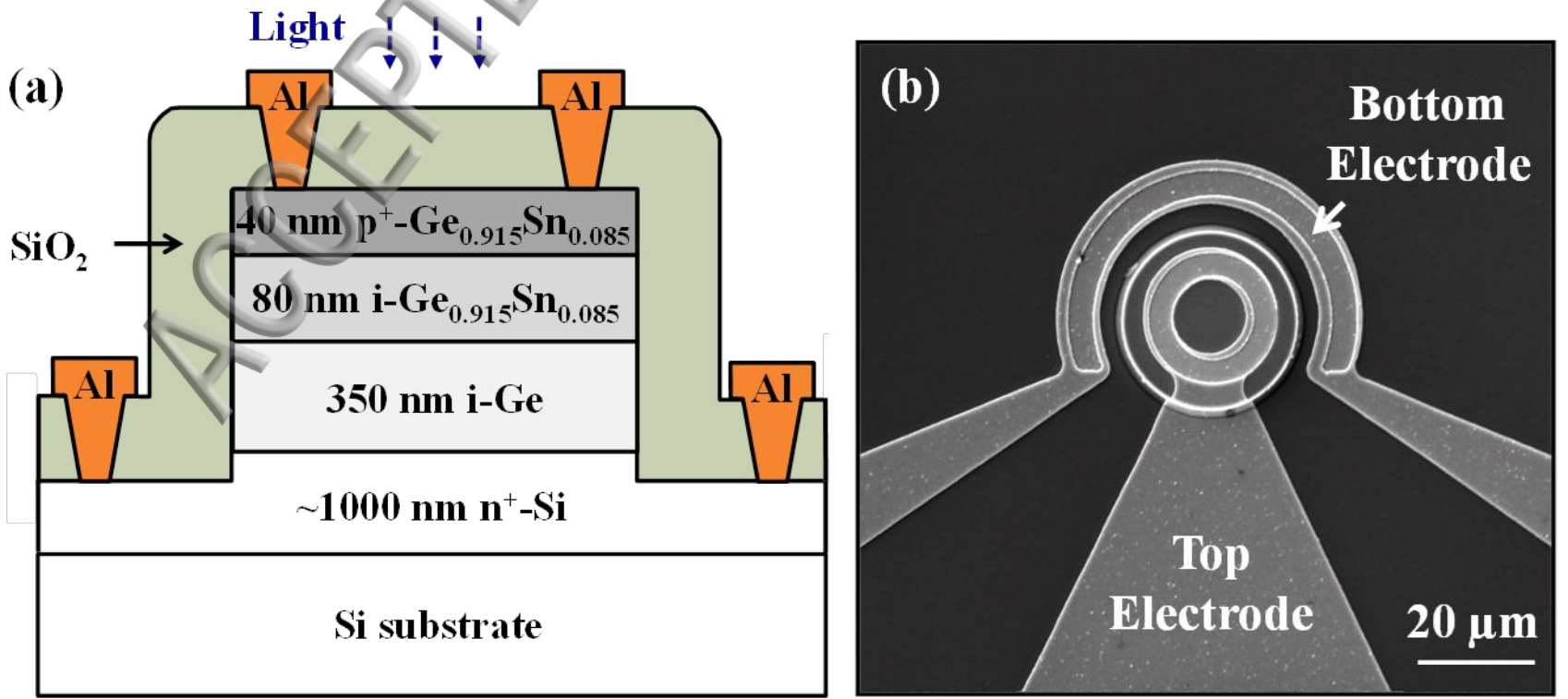
(a)
Light
Al
Al
Al
Al
SiO2
40 nm p+-Ge0.915Sn0.085
80 nm i-Ge0.915Sn0.085
350 nm i-Ge
~1000 nm n+-Si
Si substrate
(b)
Bottom Electrode
Top Electrode
20 μm

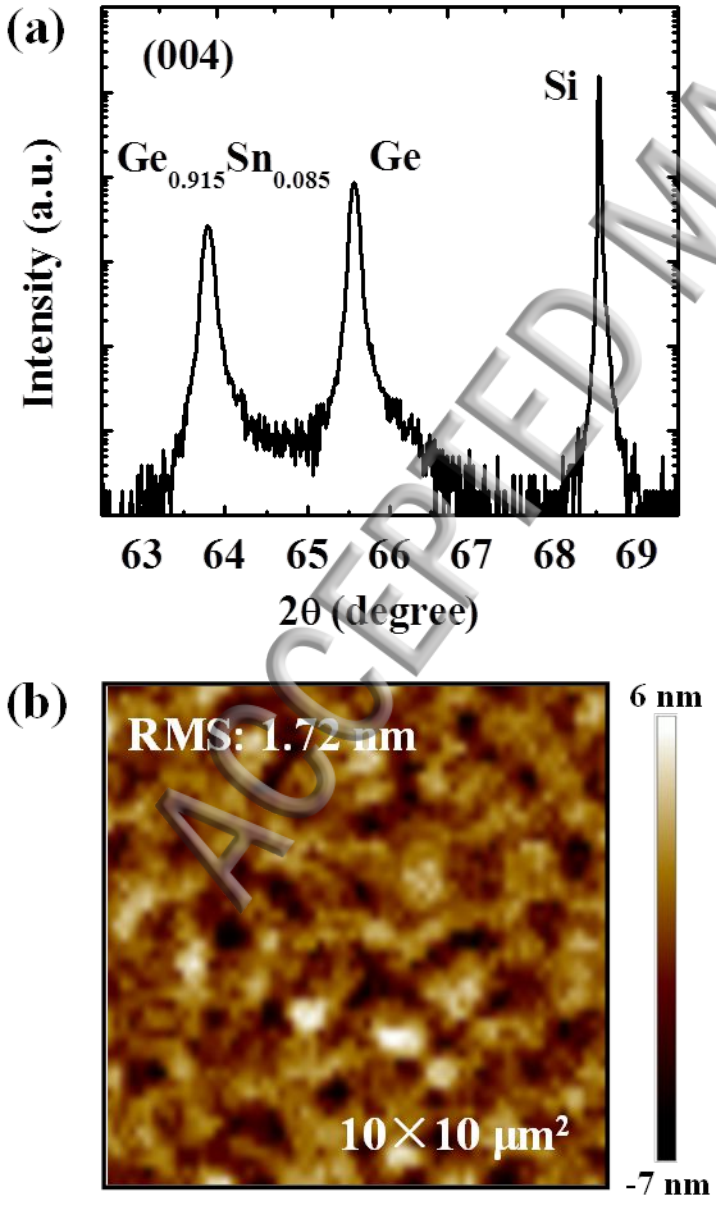
(a)
(004)
Si
Ge0.915Sn0.085
Ge
Intensity (a.u.)
63
64
65
66
67
68
69
2θ (degree)
(b)
RMS: 1.72 nm
10×10 μm²
6 nm
-7 nm

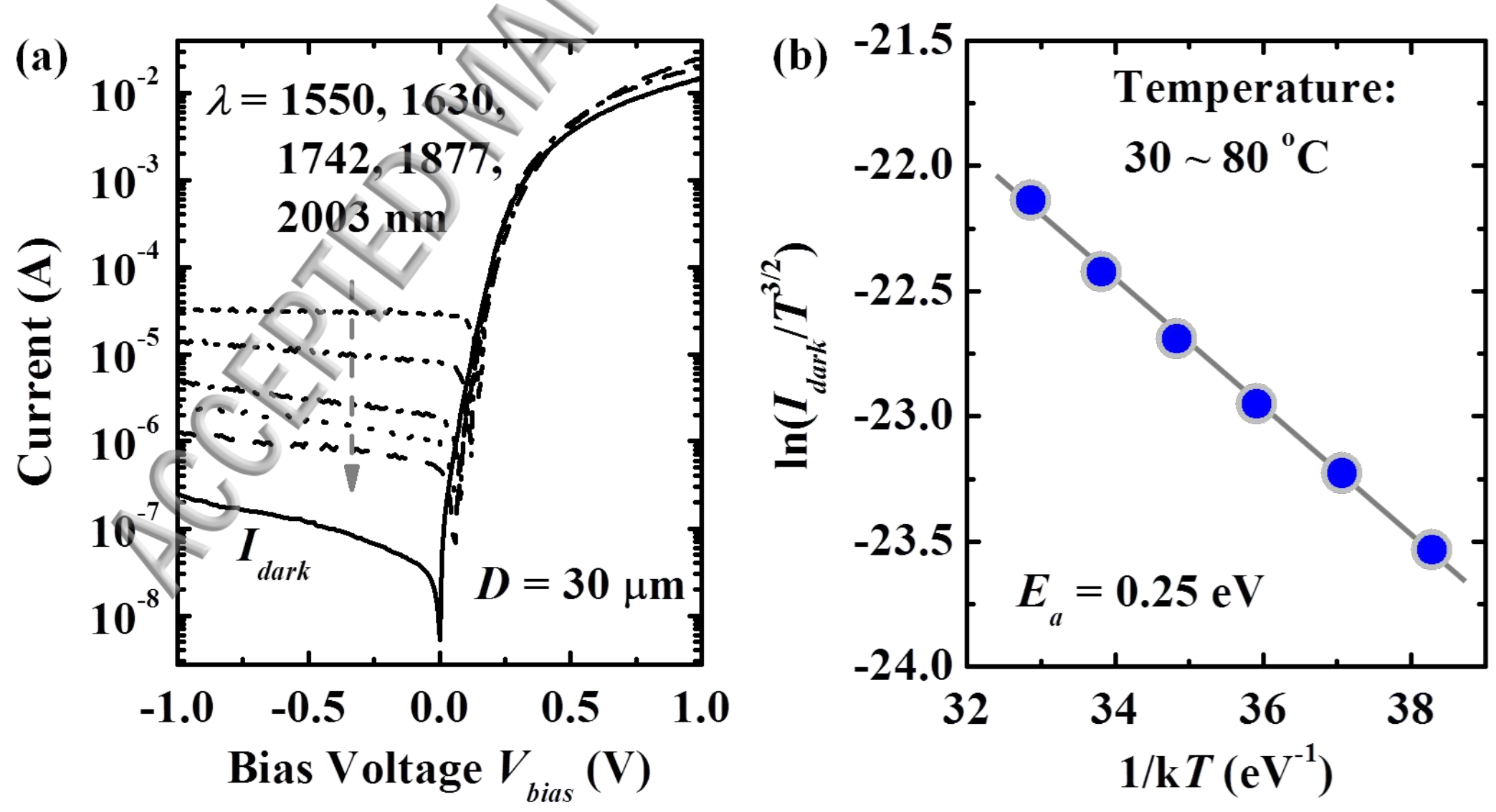
(a)
λ = 1550, 1630,
1742, 1877,
2003 nm
I_{dark}
D = 30 μm
Current (A)
Bias Voltage V_{bias} (V)
(b)
Temperature:
30 ~ 80 °C
E_a = 0.25 eV
$\ln(I_{dark}/T^{3/2})$
1/kT (eV^{-1})